MAPPING WHITE MICA IN MILLED PORPHYRY COPPER PEBBLES USING HYPERSPECTRAL IMAGERY: AN EXPLORATORY STUDY

ABIGAIL JUNE L. AGUS
March, 2011

SUPERVISORS:
Dr. F. J. A. van Ruitenbeek
MSc. W. H. Bakker

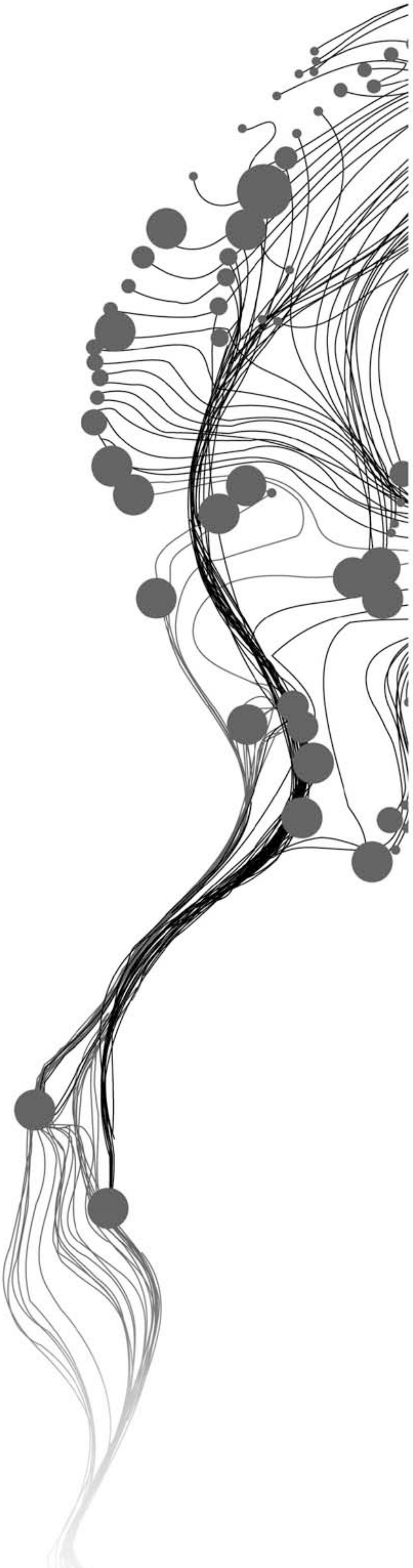

MAPPING WHITE MICA IN MILLED PORPHYRY COPPER PEBBLES USING HYPERSPECTRAL IMAGERY: AN EXPLORATORY STUDY

ABIGAIL JUNE L. AGUS
Enschede, The Netherlands, March, 2011

Thesis submitted to the Faculty of Geo-Information Science and Earth Observation of the University of Twente in partial fulfilment of the requirements for the degree of Master of Science in Geo-information Science and Earth Observation.
Specialization: Applied Earth Sciences – Earth Resource Exploration

SUPERVISORS:
Dr. F. J. A. van Ruitenbeek
MSc. W. H. Bakker

THESIS ASSESSMENT BOARD:
Prof. Dr. F. D. van der Meer (Chairman)
Dr. P. M. van Dijk (External Examiner)
Dr. M. Buxton, Anglo American (External Examiner)

ABSTRACT

Recent developments in hyperspectral sensor technology has enabled acquisition of high resolution hyperspectral images of split rock surfaces, however very few published work has dealt with this kind of data. This study investigates the use of high resolution hyperspectral images, taken using the SisuCHEMA system, to evaluate the white mica types and alteration styles present in milled porphyry copper pebbles. Spectral angle mapper (SAM) was used to classify the data yielding mineral maps of the milled pebble surface. Crystallinity, minimum wavelength and absorption depth of the white mica AlOH absorption feature at 2200nm were calculated for the hyperspectral image data and were compared to ASD point measurements. Relationship of copper concentration to AlOH parameters was also studied. Results show that majority of the white mica present in the milled pebbles have normal potassic composition based on their minimum wavelength of the AlOH absorption feature which range from 2202nm until 2213nm. Other minerals identified within the milled pebbles include tourmaline, sulphide minerals, and mixtures with chlorite and kaolinite. Spatial distribution of the different AlOH parameters allows identification of textural regions that corresponds to real geologic textures present in surface of the milled pebbles such as vein/halo and pervasive/selective alteration. Parameters calculated from ASD point measurements fall within the range of the imagery values but rarely coincide with modal values of the imagery. Copper concentration appears to be associated with short minimum wavelength; high crystallinity and deep absorption feature type white micas. Several advantages of the imagery compared to point data measurements were highlighted including delineation of alteration textures and identification of all white mica species present in the milled pebbles.

ACKNOWLEDGEMENT

I take pleasure in recognizing the following institutions and individuals for providing various forms of assistance during my study in ITC and the completion of this research:

Dr. Frank van Ruitenbeek, my first supervisor, and MSc. Wim Bakker, my second supervisor, for their critical observations and suggestions on my first ideas, preliminary results, and outputs;
Dr. Mike Buxton and Anglo American for providing the dataset used in my work and giving helpful comments on my preliminary findings;
Marinus Dalm, Jack Voncken and Tanya Law of TU Delft for sharing the results of their analyses and input during the course of this research work ;
Rainer Bärs and Harri Karjalainen of Specim Ltd. for assisting me during the sample image acquisition;
AES staff for their guidance during my stay in ITC;

I thankfully acknowledge the Erasmus Mundus Mobility for Regional Asia Programme for providing my MSc course fellowship;

I shall remember many friends with whom I shared many memorable meetings, my ERE classmates, Filipino and international friends;

My earnest gratitude to my family and Mark for their unwavering support and encouragement;

And to the Almighty Father for showering me with blessings and giving me strength in times of trial.

Abigail June L. Agus

TABLE OF CONTENTS

LIST OF FIGURES

LIST OF TABLES

1. INTRODUCTION

For the past several decades the use and development of spectral methods have been gaining momentum. It has been undertaken in variety of scales ranging from laboratory measurements to field spectroscopic studies and to a much wider coverage in airborne and satellite borne surveys. The vast amounts and different types of information that can be extracted from hyperspectral datasets have lead to applications in diverse fields including urban studies, land cover mapping, geological mapping, alteration delineation etc. (Kruse, 1998; Sabins, 1999; Hermann et al., 2001; van der Meer and de Jong, 2001). The increasingly widespread use of this method is also largely due to the rapid progress in terms of sensor development, advances in software used for analyses and faster more sophisticated computers to handle processing of these types of data (Kruse, 1998; Rajesh, 2004).

In geology, mineral spectroscopy has gradually become more prevalent especially in studies of alteration mineralization. This is mainly because common alteration minerals such as phyllosilicates, hydroxylated silicates, sulphates, carbonate and ammonium minerals have diagnostic features in the short wave infrared (1000nm-2500nm) region of the electromagnetic spectrum (Pontual et al., 1997b; Cudahy et al., 2001). The use of hyperspectral satellite imaging has enabled scientists to map alteration mineral zones over large areas with high efficiency and provided an opportunity for geologists to gain information on minerals present and discriminate lithologies even in areas that are normally inaccessible through conventional fieldwork-based methods (Cudahy et al., 2001; van der Meer, 2004). Moreover, the advent of portable field spectrometers such as the Portable Infrared Mineral Analyzer (PIMA) and Analytical Spectral Devices (ASD) Inc.'s Fieldspec Pro spectrometer has allowed field-based spectral measurements of rock units which yield spectral data that is not affected by the interference due to atmospheric effects, present in satellite and airborne imagery, that masks some of the diagnostic features of minerals in some parts of the spectrum (Pontual et al., 1997b; Yang et al., 2000; Hermann et al., 2001). This technique has provided a unique advantage of giving in depth information of alteration mineralogy in the system at a relatively fast way and a much wider scale than was previously possible with conventional chemical and XRD methods (Pontual et al., 1997b; Yang et al., 2000).

In the past few years, development of a new type of hyperspectral imaging spectrometers have been underway and have produced instruments such as HyLogger™, SisuROCK and SisuCHEMA scanners (Spectral Imaging Ltd., 2007; Mauger and Hore, 2009). These equipments combine the imaging capability of satellite and airborne hyperspectral scanners with the very high spatial and spectral resolution of point measurement field based spectrometers. They are designed to scan all types of materials including split and fresh rock surfaces, rock chips and powders. Output of these scans produces a new type of high resolution hyperspectral datasets which may have vast potential uses. Information contained in such datasets is not yet well investigated and very few published literature exists using this type of data. This may be primarily attributed to the newness of the data type coupled with the very few numbers of operational instruments and limited data availability.

In this research, hyperspectral images of surfaces of rock pebbles are analyzed which were taken using the SisuCHEMA hyperspectral scanner manufactured by Spectral Imaging, Ltd. in Finland. These rocks are milled pebbles from a porphyry copper deposit mining operation that were split into to two with the planar surface used for imaging. Ancillary data were also utilized including geochemical analysis results, thin section descriptions, ASD measurements and XRD analysis.

Porphyry copper deposits are one of the primary sources of the metal copper (Sillitoe, 2010). And copper demand around the globe has been progressively rising as a consequence of rapid industrialization which in turn puts pressure to extract more of the metal. The leading copper consumers are emerging economies such as China and India which saw a steady increase in their copper consumption. While industrialized countries such as the United States exhibit a slight decline in their consumption and was overtaken by China as the biggest refined copper consumer in 2002, with an estimated refined copper import of 1.1 million tons in early 2009 (United States Geological Survey, 2010). To ensure continuous copper supply, exploration programs are in place to look for new copper deposits to meet the future needs of the industrialized world.

As part of exploration, several stages of geological information gathering are undertaken including lithological description, mineral mapping, drilling etc. These would require intense work in identifying the different rocks and minerals present in the prospect area. It is in this aspect that the use of hyperspectral methods will greatly facilitate acquiring the required relevant mineralogical information which can then aid in better understanding of the geologic system thus helping in identifying prospective economic mineral deposits.

1.1. Problem Description

Few studies have been conducted and fewer literature have been published that documents the use of hyperspectral images of rock surfaces and the different information it may contain (Mauger and Hore, 2009). This may be because of the limited availability of the data which stems from the relative newness of the instruments as well as its few numbers. The SisuCHEMA system was originally designed for chemical imaging but still cover the same SWIR region that contains diagnostic absorption features of minerals (Spectral Imaging Ltd., 2007). Thus there is a need to examine this type of data and explore what geological information we can get out from this images which may include, in this case, identification of minerals present in the samples, their distribution, as well as the variability in mineral types and the texture pattern they exhibit. The study of the distribution of minerals and their different types has implications to the different geologic processes undergone by the rocks, particularly stages of alteration (Taylor, 2009). The mineral assemblage encountered in rocks essentially represents the physico-chemical conditions of the system at the time of its formation and studying these minerals provides critical geologic information for understanding the different processes undergone by the system (Pirajno, 2009). Further, because of its nature as an imagery dataset, measurements are taken from contiguous areas covering the whole pebble and because of its high spatial and spectral resolution, compositional variations will be easily determined and patterns may be delineated which may be otherwise indistinguishable through conventional methods of analysis or hyperspectral point measurements. Analysis of patterns in composition variation can correspond to physical properties in the samples such as alteration textures. Identification of compositional variability is one of the advantages of using hyperspectral methods especially in determining the range of white mica composition since distinct absorption features and differences of its parameters such as wavelength of the main 2200nm absorption feature is correlated to changes in its chemistry (Duke, 1994; Yang et al., 2001; Duke and Lewis, 2010).

Moreover, most of the studies that have been conducted have dealt mainly with gold deposit regions and were imaged using the Hylogger™ system built in Australia (Huntington et al., 2004; Mauger and Hore, 2009; Huntington et al., 2011). Researches in porphyry copper systems using high resolution hyperspectral imagery data from similar scanners have not yet appeared in the literature. Thus there is a need to determine the usefulness of this data within this kind of geologic environment.

Last, the use of field based hyperspectral point measurements have been widely documented and have provided good results in the study of alteration mineralization (Kruse, 1998; Yang et al., 2001). With this precedent, it is also important to determine the added value of using imagery as opposed to the more common point measurements in terms of the amount and type of geologic information that can be gained.

1.2. Research Objectives

This research is an exploratory study into the different types of geologic information (mineral composition and alteration texture) that may be present in high resolution hyperspectral imagery of milled pebbles from a porphyry copper deposit. It aims to identify the different minerals, especially white mica, that are present in the pebbles and establish whether patterns of spatial distribution can be delineated using this type of imagery then relate these patterns to observed alteration textures in the milled pebble samples.

1.2.1. Specific Objectives

To achieve the above mentioned general objective, the following specific objectives were planned:

- To identify the diagnostic absorption features present in the data thereby distinguishing the different minerals present in the pebbles
- To determine the types of white mica composition and crystallinity present in the pebbles based on the parameters of the AlOH absorption feature at 2200nm
- To compare the hyperspectral images to ASD point measurements taken from different areas on the milled pebbles surface
- To identify alteration textures, vein/halo and pervasive/selective alteration, observed in the rock samples by using hyperspectral imagery derivative (white mica AlOH parameter images)

1.3. Research Questions

The research questions for this study are as follows:

1. What minerals are present in the pebbles and how are they spatially distributed?
2. What is the range of the minimum wavelength of the AlOH absorption feature of white mica in the milled pebbles?
3. How do the AlOH parameters (minimum wavelength, crystallinity and depth) values calculated from the ASD point measurements compare with the range of values calculated for the whole hyperspectral images?
4. What are the white mica types, as characterized by the AlOH parameters, present in the milled pebbles with high copper concentrations?
5. Do image textures in the hyperspectral data derivatives, AlOH parameter images, represent actual alteration textures (vein/halo and pervasive/selective alteration) in the milled pebble surface?
6. What are the advantages of using hyperspectral imagery compared to point measurements?

1.4. Scope and Limitations of the Research

The pebbles used for this research were uncrushed parts of milled ore rocks from an Anglo American porphyry mining operation. Figure 1 shows a flowchart of the mine operation and the dashed circle indicates the stage in the operation where the pebbles used were taken. In normal mine operation, these pebbles will be segregated from the milled ore and will be considered as waste. However, some of these pebbles are still mineralized and contains more than 0.4% copper which is the mine cut-off grade. Segregating the payable milled pebbles from the unmineralized ones using ASD point measurements is the topic of another research by Mr. Marinus Dalm from TU Delft. The samples used for this research is a subset of Mr. Dalm's pebble samples. And the study conducted is mainly focused on the hyperspectral image analysis and extracting relevant geologic information from these images. Point spectral measurements from ASD, taken by Mr. Dalm, were analyzed mainly for preliminary characterization of the minerals and comparison of spectral features to that of the imagery spectra. In addition, given the fact that these are milled pebbles, exact coordinate locations of their sources are not available and geologic information correlation between different pebbles are limited.

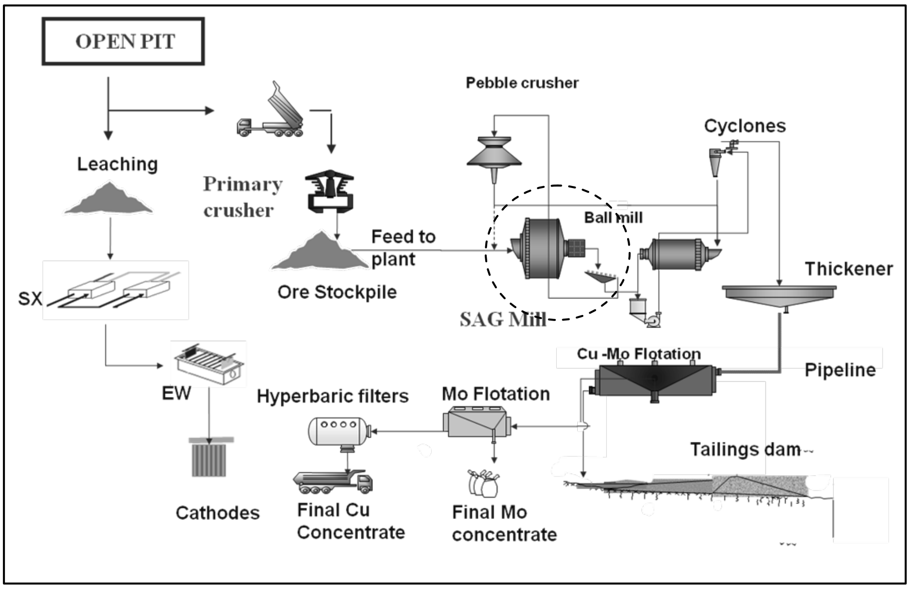

Figure 1. Flowchart of porphyry copper mine operation. Pebbles used for this research are uncrushed ore from the milling stage (dashed circle)

1.5. Research Approach

The research first analyzed individual spectra of the ASD measurements then the image end members. The ASD analysis was done mainly to provide a comparison of the different mineral spectra obtained to that of the spectral characteristics of imagery endmembers. Also copper concentration modelling using multiple linear regression was calculated to provide preliminary information of the relationship between the different AlOH absorption feature parameters.

The hyperspectral image processing consists of several steps designed to answer the different research questions and achieve the research objective (Figure 2). After image cropping to remove the background, endmember identification was done leading to classification via spectral angle mapper. This step generated mineral maps for each pebble. Calculating the AlOH parameters, white mica variability maps were created which shows white mica composition differences based on absorption minimum wavelength, depth and crystallinity which help in delineating spatial patterns of compositional variability. Image analyses were then undertaken to examine the patterns of spatial distribution of minerals, white mica types based on the AlOH parameters and identification of alteration textures. To investigate the relationship of copper enrichment to white mica type, the mode of the different parameter images were identified for each milled pebble sample. Thin section and XRD results were also used to validate the results of the image analyses done.

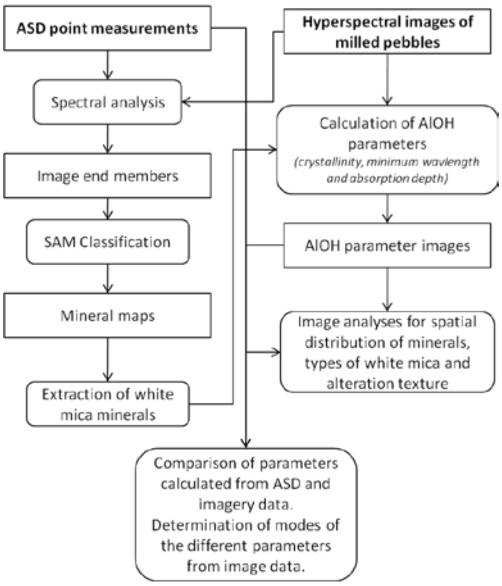

Figure 2. Overview of the research steps undertaken

1.6. Thesis Structure

This thesis report is divided into five (5) chapters with the titles and descriptions of their content shown below.

Chapter 1. Introduction	-This chapter is an overview of the whole research work containing the different objectives, research questions and a description of the overall flow of the research.
Chapter 2. Background	-This chapter compiles the different relevant published information relating to the study.
Chapter 3. Methodology	-The different types of datasets utilized during the whole of the research as well as their descriptions are contained in this chapter. Also general methodologies applied to the datasets are detailed.
Chapter 4. Results of Spectral and Image Analyses	-This chapter presents the results of the spectral and image analyses conducted including the results of mineral classification done.
Chapter 5. Conclusions	-Presents the conclusions derived from the results of the study
Chapter 6. Recommendations	-Contains recommendations for further research

2. BACKGROUND

This chapter presents a collection of relevant information connected to the thesis topic. Discussions about the definition and nature of porphyry deposits are included as well as descriptions of the common alteration mineral assemblage that can be found in the system. A description of the geology of Los Bronces porphyry deposit is presented. An updated summary on how hyperspectral methods are used for mineral identification is also given, including current techniques used for interpretation, mapping etc. This is then followed by explanations regarding the definitions of the different terms used especially the differentiation between geologic, alteration and image textures together with details on how they can be related.

2.1. Porphyry Copper Deposits

Originally the term porphyry copper was used to refer to large low grade copper deposits were mineralization is dispersed throughout the rock units (McMillan and Panteleyev, 1980). Another more precise definition is given by Guilbert and Park (1986), these are large low- to medium-grade deposits of predominantly copper and molybdenum that are spatially as well as temporally associated to calc-alkaline porphyritic intrusions. They are commonly encountered within magmatic arcs formed above active subduction zones at convergent plate boundaries although a small percentage are known to exist in post collision and other tectonic settings (Sillitoe, 2010 & references therein).

Historically, copper mining have been widely practiced since 1800's and the well known copper mining region in Chile have been mined even before the Spanish started mining operations in the area at around 1601. However, it was not until 1905 that the porphyry copper era started, with countries like the United States and Chile leading production (Bateman, 1955). Today, ore extracted from porphyry copper systems accounts for nearly three quarters of the world copper supply. In addition, the systems also contain other economic metal concentrations such as molybdenum, gold, silver, zinc, lead and others (Sillitoe, 2010).

Common ore grades found in these systems range from 0.5% to 1.5% copper with reserves at the scale of millions of tons. The largest known economically extractable reserve is Los Bronces-Rio Blanco located in Chile with 203 million tons (Sillitoe, 2010). Mining operations within this deposit is currently being operated by Anglo American. Minimum tonnage for porphyry deposits are in the order of 100 million tons. Such large deposits usually cover areas of 1-2 km^2 although alteration signatures may be encountered within areas of 10 to 20 times larger than the target deposit (Guilbert and Park, 1986).

Figure 3 presents a telescoped view of the anatomy of porphyry deposits and its relationship with the surrounding rocks and deposits. Sillitoe (2010) in his article, tackling field based geology of porphyry systems, provides a comprehensive discussion of this model. For the scope of this thesis, it is significant to note the central location of porphyry copper deposits with distal mineralization of different metals including gold, zinc, lead, and silver. Porphyry systems also show a marked tendency to occur in linear belts typically parallel to orogenic belts similar to that in northern Chile. Further, faults and fault intersections are frequently involved in varying degrees in determining the location and geometry of the resulting deposit. Based on different field observations, varying relationships exists between the intrusive pluton and the porphyry copper but typically the intrusives are multiphase with substantial time gaps between magma advances. Magmatic-hydrothermal and phreatic breccias are also very common which results from the release of over pressured magmatic fluids. The presence of low permeability host rocks which magmatic fluid cannot penetrate may lead to blind deposits of high grade ore (Sillitoe, 2010 & references therein).

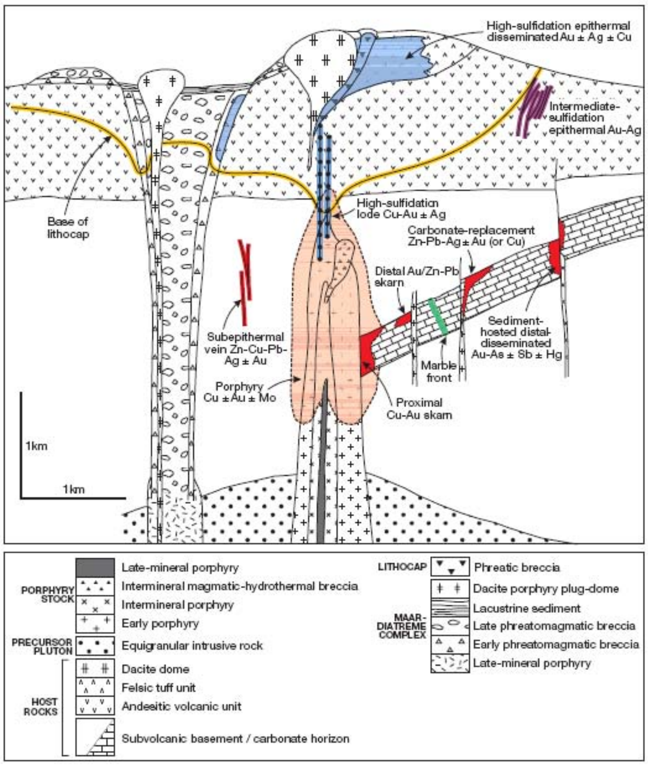

Figure 3. Anatomy of centrally located Cu porphyry deposit showing its relationship with surrounding rocks and other mineralization ((Sillitoe, 2010)

2.1.1. Zones of Alteration and Sulphide Occurrences

Hydrothermal alteration occurs when hot fluids (hydrothermal fluids) pass through rocks which results in addition, removal or redistribution of the rock components. This change occurs because the pre-existing rocks are not in equilibrium with the hydrothermal fluids, thus to re-establish equilibrium, new mineral assemblages are formed which produces changes in rock grain size and texture. In this respect, the effected changes (mineralogy, grain size and texture) represents the physico-chemical conditions of the system (Pirajno, 2009). For porphyry systems this process may occur in several cycles depending on several factors including timing of magma advance, rock permeability etc. As a consequence, each cycle may produce different mineral assemblages and signatures, depending on wall-rock composition, temperature, pressure, and fluid chemistry which then may be subjected to another alteration pulse further changing its constituent minerals. This process is called overprinting which commonly occurs in porphyry copper deposits and produces a lot of variability in terms of alteration assemblages within the system.

Porphyry copper deposits typically exhibit consistent broad-scale alteration mineralization zoning pattern which in most of the deposit exists coaxially with the deposit and extends concentrically outward (Guilbert and Park, 1986; Sillitoe, 2010). This alteration affects large areas around the main deposit and can extend to several cubic kilometres.

A generalized schematic is presented in Figure 4 showing the different alteration phases that are found in the porphyry system. Centrally from bottom upward, potassic alteration, close to the intrusive stock, chlorite-sericite, sericitic alteration and advanced argillic. Field observations have also noted that shallow alteration types consistently overprint the deeper alteration zones. Marginal areas of the deposit often develop chloritic and propylitic alteration at shallow and deeper levels, respectively (Sillitoe, 2010). Common mineral assemblages of these alteration zones are presented in Table 1.

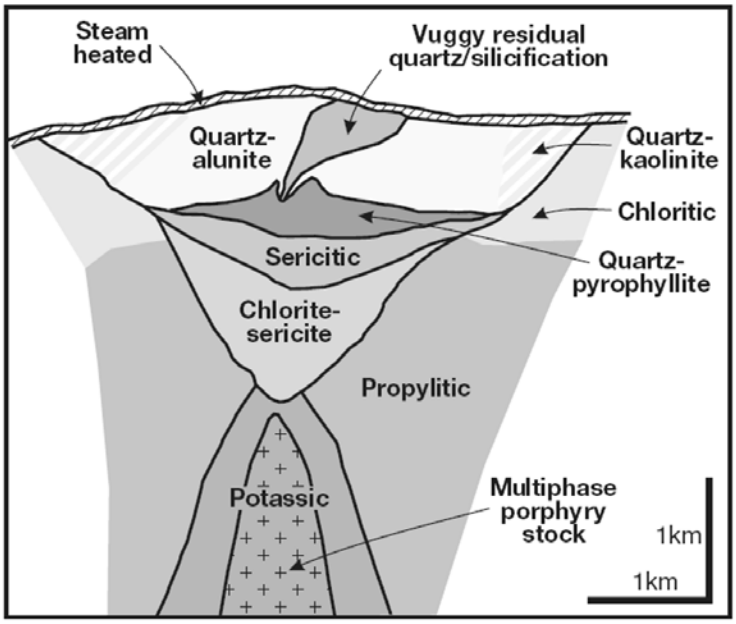

Figure 4. Schematic diagram of generalized alteration zones within porphyry copper systems (Sillitoe, 2010)

Table 1. Alteration types found in porphyry Cu and their mineral assemblage

Alteration type	Key Minerals	Economic Potential
Potassic (K-silicate)	Biotite, K-feldspar	Main ore contributor
Propylitic	Chlorite, epidote, albite, carbonate	Barren, except for subepithermal veins
Chlorite sericite (sericite-clay-chlorite)	Chlorite, sericite/illite, hematite	Common ore contributor
Sericitic	Quartz, sericite	Commonly barren but may constitute ore
Advanced argillic	Quarts, alunite, pyrophyllite, dickite, kaolinite	Locally constitute ore in lithocaps and their roots

One of the most prevalent hydrothermal alteration mineral in porphyry systems is white mica which is composed of mixtures of fine grained mica with compositions ranging from muscovite, celadonite and illite (van Ruitenbeek et al., 2005). Studies have shown that variations of the different characteristics and composition of white mica provides insights into the hydrothermal activity that produced these minerals (Pirajno, 2009). Different factors affect the crystallinity of illites which includes water content, crystal defects and potassium content where increase in water content and decrease in potassium correspond to lower crystallinity values (Meunier and Velde, 2004).

2.2. Geology of Los Bronces Deposit, Chile

Los Bronces and its neighbouring deposit Rio Blanco hosts one of the largest extractable porphyry – hosted copper-molybdenum deposit in the world. It has a total estimated reserve of 203 million tons. It is located on the west side of the Andes within the Miocene-Pliocene metallogenic province of central Chile (Figure 5). Two companies are currently operating in this area, Codelco in Rio Blanco and Anglo American in Los Bronces (Davidson et al., 2005).

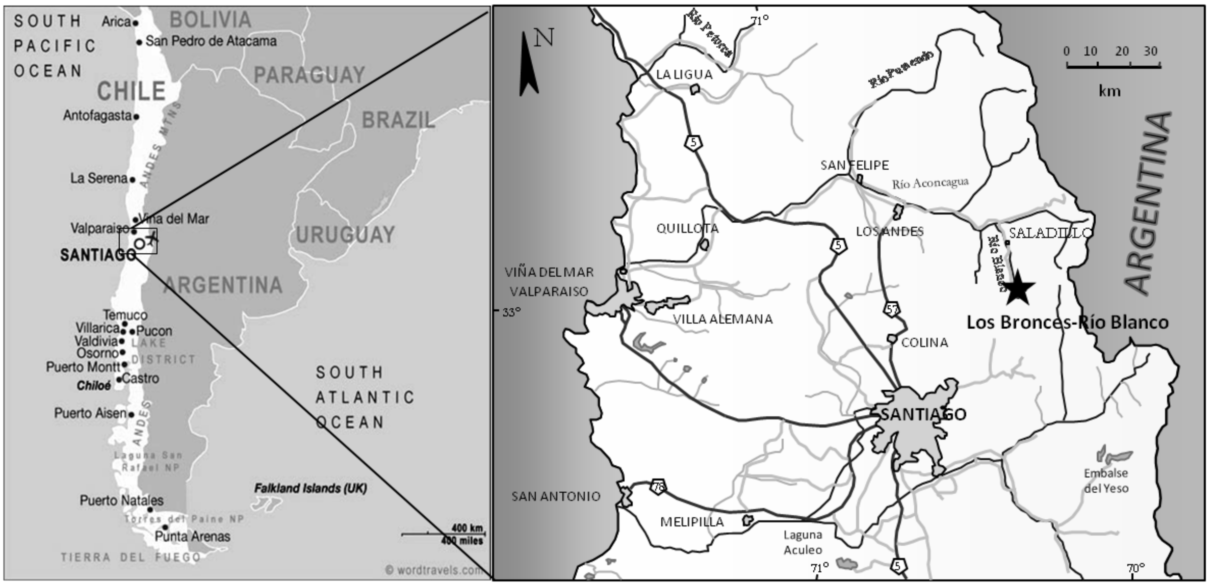

Figure 5. Location map of Los Bronces-Rio Blanco deposit, Chile

A comprehensive description of the geology of the area is given by Warnaar et al. (1985) and a brief summary is given here. The immediate surrounding area of the deposit is underlain by the Miocene Farellones Formation which overlies the Cretaceous-Tertiary marine strata that has been covered by continental volcanic rocks and has undergone significant deformation, uplift and erosion. The Farellones Formation is composed of andesite flows and pyroclastics interbedded with continental sediments. A widespread event of intrusive magmatism formed numerous intrusions within this volcanic terrain which includes the Francisco Batholith which hosts the two porphyry copper deposits. This porphyry copper system is oval-shaped with the longest axis trending northeast. Los Bronces deposit is hosted by the hydrothermal copper-tourmaline breccias which were emplaced in and superimposed on the earlier porphyry system. A post mineral volcanic neck or diatreme, La Copa, removed significant part of the center of the initial porphyry. During the waning or after the copper mineralization, dacite, latite and quartz porphyries were then emplaced towards the southern and northern areas. Figure 6 shows the geologic map of Los Bronces-Rio Blanco District.

The Los Bronces-Rio Blanco copper porphyry system is mainly hosted within the San Francisco Batholith which is largely composed of quartz monzonite and quartz monzodiorite. Seven tourmaline breccias are associated with this deposit and form the most favourable host rocks for copper and molybdenum mineralization. These are Ghost, Central, Western, Infiernillo, Anhydrite, Fine Grey and Donoso Breccia (Fig. 7). These breccias are not fully explored at depth but are known to extend below 3,050m and on the surface they are observed to be interfingering and coalescing with each other.

Hydrothermal alteration includes propylitic, sericitic, silicic and potassic alteration phases. Generally clasts of tourmaline breccias were not altered during breccias formation. The degree of alteration in these rocks are mainly influenced by their location in reference to the earlier formed porphyry system where breccias to the west central part exhibiting strong quartz-sericite alteration whereas those in the northern part show weak to moderate propylitic alteration.

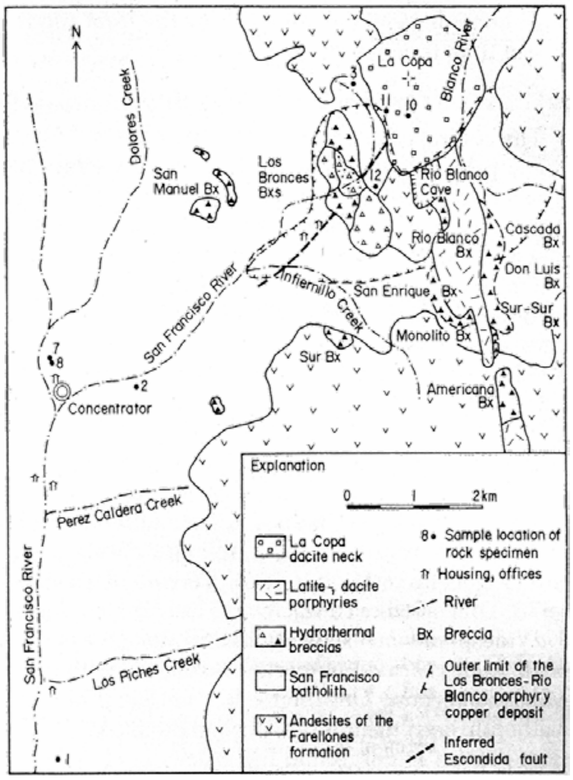

Figure 6. Simplified geologic map of Los Bronces-Rio Blanco area modified from Irarrazaval et. al (1979) and Stambuk (1982).(Warnaars et al., 1985)

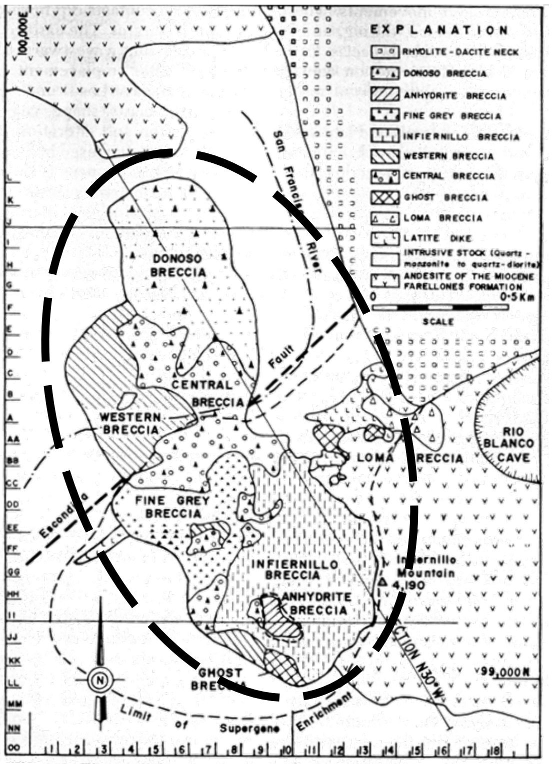

Figure 7. Simplified outlines of Los Bronces breccias (Warnaars et al., 1985). Heavy dashed line outline the final pit operation of Los Bronces mine.

Mineralization in the area is best known within the Donoso Breccia which has been mined since 1864. Sulphides in the matrix include chalcopyrite, pyrite and specularite which are sporadically distributed within the rocks and forms irregularly shaped shells in open pit mining level. This makes grade estimation challenging as transitions between shells may be rapid. Moreover, secondary enrichment is economically important because it enhanced the primary copper grades within the southern two thirds of the Los Bronces breccias complex.

2.3. Hyperspectral Methods for Mineral Identification and Mapping

For the past several decades, spectral investigations of minerals have been routinely conducted in several areas of geological research, mapping and exploration. These have been undertaken at different scales both spatially and spectrally with hyperspectral data providing the highest spectral resolution and range from VNIR, SWIR and TIR (Sabins, 1999). Spectral characteristics of different minerals have been established from several studies and techniques for processing such types of data have proliferated in the field, facilitating the utility of this method. Hyperspectral data is also especially suited in the study of alteration mineralization particularly because clays and other alteration minerals have very good diagnostic absorption features at these regions (Hunt and Ashley, 1979). In this research, high spatial and spectral resolution hyperspectral datasets of split rock pebbles are used to study the alteration mineralogy of a porphyry copper deposit. Several minerals within the different porphyry copper alteration zones contain diagnostic absorption features evident in their reflectance spectra (Pontual et al., 1997a).

Most of these minerals have distinct features found at several regions along their SWIR spectra which are caused by absorption of light by their individual chemical components through two main processes, charge transfer and vibrational processes. In alteration mineralization, charge transfer absorptions commonly involve metal compounds where inter-element transition occurs when the absorption of a photon causes an electron to move between ions or between ions and ligands in the mineral. On the other hand, vibrational absorption features are produced by dipole components of minerals that vibrate along their chemical bonds (Clark, 1999). Although most of the molecular vibrations have fundamental (primary) absorption features located at the mid infrared region, absorption features observed in the SWIR are multiples of the fundamental vibration frequency called overtones (Pontual et al., 1997b).

In the shorter wavelengths, one of the more obvious absorption features is found in the 1400nm region which is attributed to vibrational stretching of the OH bond in minerals. The combination stretching of OH and bending of H-O-H bonds also produces overtones along the 1900nm which is commonly found in hydrated minerals (Clark, 1999). One common charge transfer absorption feature in alteration of porphyry systems is due to Fe^{2+} and Fe^{3+} transitions. Specifically, the main absorption is centred within the ultraviolet region. However, wings of this feature may influence the visible and SWIR regions (Hunt, 1977). Another region which contains important diagnostic absorption features is the 2200nm-2500nm which is mainly caused by metal-OH stretching and bending (Hunt and Ashley, 1979; Duke, 1994; Clark, 1999). This is where several of the alteration mineralogy present in porphyry systems exhibit diagnostic absorption characteristics.

Figure 8 presents the spectra of some common alteration minerals found in porphyry copper deposits and are predominant in the milled pebble samples. The chief alteration mineral in porphyry deposits is white mica which includes illites and muscovites. These two minerals are distinguished through their diagnostic AlOH absorption at 2200nm with several secondary features at 2340nm and 2440nm. In addition, OH and water overtones at 1400nm and 1900nm are characteristic (Clark, 1999; Yang et al., 2001). Chlorite and kaolinite are also common which are identified through their 2240nm and 2340nm absorptions which are due to MgOH for chlorites while a doublet in the 2160nm and 2200nm is diagnostic for kaolinites (Pontual et al., 1997b). Another mineral commonly found in porphyry systems is tourmaline which is indicative of Boron bearing fluids in the system and is identified by a series of absorption features located at 2200nm, 2245nm, 2300nm and 2360nm (Bierwirth, 2004).

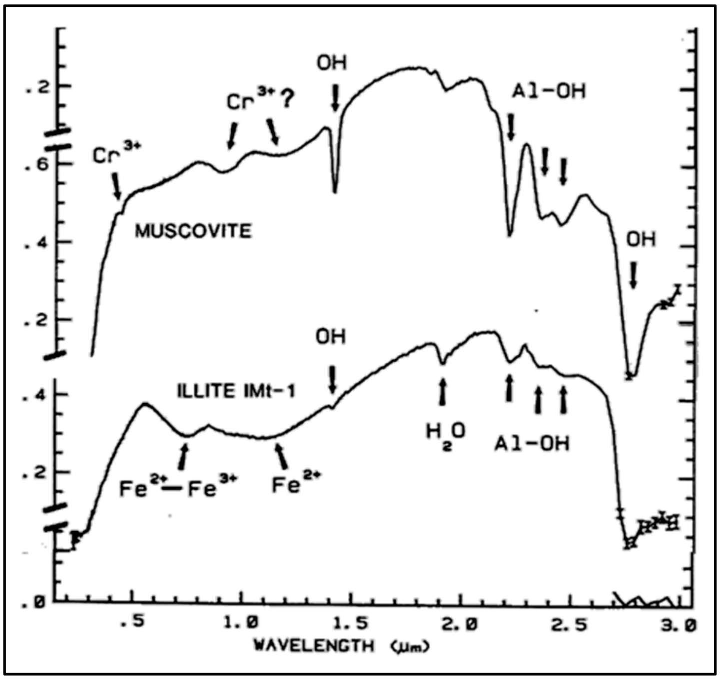

Figure 8. Muscovite and illite spectra, common alteration minerals in porphyry copper systems, with different absorption features and the chemical components that causes them (Clark, 1999)

Aside from mineral identification, spectral studies have also been proven to approximate mineral chemical composition variability, crystallinity and semi-quantitative measurements of abundance (Cloutis, 1996; Hermann et al., 2001). Research by Duke (1994) shows that variability in muscovite compositions which is attributed to Tschermak substitutions of Al and Si with Fe/Mg in there chemical structures yields consequent band shifts in the 2200nm absorption feature. This shift can either be towards the shorter wavelengths for more Al rich muscovites or to the longer wavelengths for increasing Fe/Mg contents (Duke, 1994; Clark, 1999; Yang et al., 2001). Such changes in minimum wavelengths for the 2200nm feature has been increasingly investigated to be used as guides to exploration since the chemical substitution itself, in relation to the shift in the absorption feature position, is greatly controlled by the delicate interplay of chemical and physical conditions of the alteration system and thus may provide valuable information with regards to mineralization conditions (Yang et al., 2001).

Several field studies have been conducted using the different parameters of the primary AlOH absorption feature at 2200nm to approximate the variability of white mica composition. In Wairakei geothermal system, Australia, the work conducted by Yang et al. (2000) looked into the different hydrothermal minerals present in the system and their zonation. They were able to identify illites with compositionally insignificant Fe or Mg contents and determine at what depths it becomes proportionally dominant in the system. These absorption parameters have also been used to study and delineate patterns in low-grade metamorphosed rock in Bel Super group, Idaho which correlates to depth of burial and later structural deformation (Duke and Lewis, 2010). Brown et al. (2006) used minimum wavelength maps of the same absorption feature for muscovites to investigate the patterns of composition variation in North Pole Dome, Pilbara Craton, Australia. These parameters have also been employed to map fluid pathways in fossil hydrothermal systems in Western Australia (van Ruitenbeek et al., 2005). Moreover, an analysis of these spectral feature parameters was done by van der Meer (2004) and he proposed a linear interpolation method in calculating these parameters. Minimum wavelength parameter derived from multiple linear regressions of select band ratios of hyperspectral imagery has also been used to study the spatial distribution of white mica variation (van Ruitenbeek et al., 2006).

Aside from using the different absorption parameters of the AlOH, several spectral matching algorithms have been developed to map mineralization in different areas. One of the more commonly used is the spectral angle mapper (SAM) which is frequently available in standard image analysis software. This method of classification has been tested to perform well, attaining high classification accuracies using different types of hyperspectral data and classifying different materials not only mineralogy and lithology. Several workers have implemented this method in studying land cover, vegetation species, water bodies, lithology etc. (e.g. South et al., 2004; Chen et al., 2007; Hestir et al., 2008). SAM works by projecting the different image values as vectors in N-dimensional space where N is the total number of bands present in the image. It then does the same to the reference spectra and computes the angle between the two vectors, unknown pixel from the image and known reference spectra. The similarity measure is taken from the angle of the two vectors, where the smaller the value obtained the higher likelihood that the two materials are the same. During classification, the image pixel will be assigned the class where it has the smaller angle with the class reference spectra. Several geological applications have also been made using the SAM algorithm. These include mapping ultramafic lithologies using ASTER data in Australia and using AVIRIS together with MASTER in Cuprite, Nevada (Rowan et al., 2005; Chen et al., 2007).

2.4. Texture

In this research, the term texture refers to two distinct but related concepts. The first one is geologic texture, specifically alteration texture, and the other is image texture. Textures in geology refers to rock texture which is the visible characteristics of a rock that includes its grain size, grain orientation, rounding, angularity or presence of vesicles etc. (Kurniawan et al., 2009). Alteration texture is a subdivision under geologic textures which encompasses those textures that are superimposed on the rock due to the process of alteration such as hydrothermal alteration (as the case of samples used), dissolution, diagenesis, metamorphism and deformation (Gifkins et al., 2005). As image textures are products of the responses of the physical surface being imaged, alteration textures are strongly related to image textures, which can be a functional tool to indirectly study the different alteration textures.

Terminologies used to describe alteration texture can be confusing because of the inherent subjectivity in their identification. Descriptions of alteration facies usually include mineral assemblage, intensity and style of alteration. Terms like weak, moderate and strong are commonly used to denote alteration intensity. In this research, three styles of alteration are considered which include vein-halo, pervasive and selective. Vein-halo type alteration is characterized by narrow zones of alteration which are adjacent to completely or partially infilled fractures, intrusion contact or stratigraphic contacts (Gifkins et al., 2005). Pervasive alteration is characterized by replacement of most or all pre-existing minerals which results into partial or complete obliteration of the original textures (Pirajno, 2009). While selective alteration refers to preferential replacement of the original minerals (i.e. chlorite replacing biotite and white mica replacing feldspars) wherein original textures may only be slightly modified (Gifkins et al., 2005).

3. METHODOLOGY

This chapter describes the different datasets that were used during the research study. It also discusses the different methods that have been used for the different analyses conducted in order to answer the different research questions put forward to achieve the proposed objectives.

3.1. Datasets

The primary dataset that was used for this research were high resolution hyperspectral images of milled copper pebbles taken using the SisuCHEMA imager of Spectral Imaging Ltd. (SPECIM), Finland. The rocks that were imaged are uncrushed porphyry copper milled pebbles. These pebbles are the remaining materials from copper ores that were not pulverized during milling in mining operations. Normally, these would then be discarded as waste however some of these pebbles still contain significant copper concentrations, greater than 0.4% Cu (mine grade cut-off). Sorting the high grade ore from waste using ASD spectral point measurements is a topic of another research being conducted by Mr. Marinus Dalm from TU Delft. A total of 50 samples were imaged, a subset of the whole 150 pebbles used by Mr. Dalm, and of this seven samples were chosen based on their copper concentration and textural features. These samples were then used for the several image analyses conducted. Sample numbers were retained from the original 150 pebbles.

The pebbles were imaged using the SisuCHEMA system which was originally designed for chemical imaging but is flexible enough to mount rock samples on its imaging tray. It covers the SWIR region of the spectrum which is appropriate for studies of alteration mineralization. Figure 9 presents the different performance specifications of this instrument. It should be noted that the sensor used during the imaging of the samples covers the 1000nm-2500nm spectral range and the spatial resolution is 0.21mm/pixel.

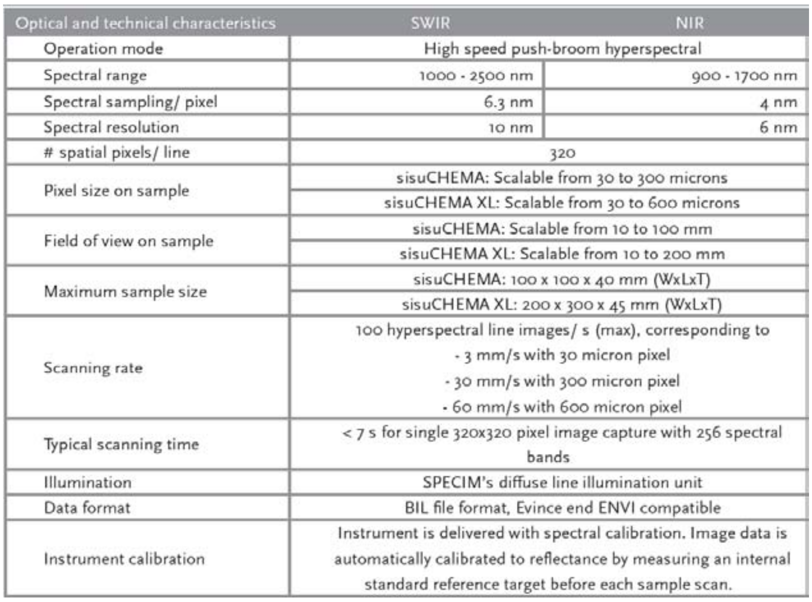

Optical and technical characteristics	SWIR	NIR
Operation mode	High speed push-broom hyperspectral	
Spectral range	1000 - 2500 nm	900 - 1700 nm
Spectral sampling/ pixel	6.3 nm	4 nm
Spectral resolution	10 nm	6 nm
# spatial pixels/ line	320	
Pixel size on sample	sisuCHEMA: Scalable from 30 to 300 microns sisuCHEMA XL: Scalable from 30 to 600 microns	
Field of view on sample	sisuCHEMA: Scalable from 10 to 100 mm sisuCHEMA XL: Scalable from 10 to 200 mm	
Maximum sample size	sisuCHEMA: 100 x 100 x 40 mm (WxLxT) sisuCHEMA XL: 200 x 300 x 45 mm (WxLxT)	
Scanning rate	100 hyperspectral line images/ s (max), corresponding to - 3 mm/s with 30 micron pixel - 30 mm/s with 300 micron pixel - 60 mm/s with 600 micron pixel	
Typical scanning time	< 7 s for single 320x320 pixel image capture with 256 spectral bands	
Illumination	SPECIM's diffuse line illumination unit	
Data format	BIL file format, Evince end ENVI compatible	
Instrument calibration	Instrument is delivered with spectral calibration. Image data is automatically calibrated to reflectance by measuring an internal standard reference target before each sample scan.	

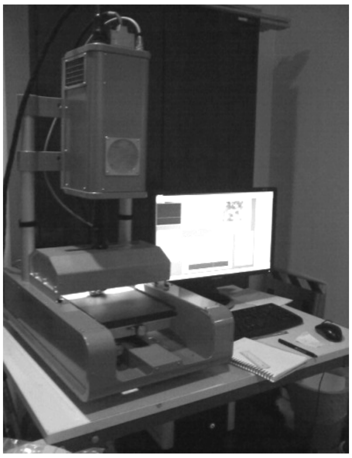

Figure 9. Performance specifications of the SisuCHEMA imager used to acquire the hyperspectral images of milled copper pebbles (Spectral Imaging Ltd., 2007), left; photo of the instrument, right

Several ancillary data were also utilized during this research. These are the following:

1. XRF chemical analysis results for 31 samples for Cu and 32 other elements
2. Thin section results for 5 samples
3. XRD analysis results for 25 samples
4. ASD point measurements

3.2. Image Analyses

3.2.1. Mineral Mapping

Prior to any analysis undertaken, careful examination of the image data was done to familiarize with the different minerals that may be present in the sample. Colour composite images using bands 144/208/202 (RGB) was used to help identify possible areas which contain different minerals. This was then followed by selection of representative endmember spectra from the images coupled with the information provided from XRD, ASD point measurements and thin section results to confirm the presence of each mineral. Different sets of endmember spectra were generated for each image as varying minerals are present in each milled pebble. This was also done to ensure maximum accuracy during spectral matching in the classification stage.

Spectral Angle Mapper (SAM) algorithm was used to classify the hyperspectral data yielding mineral distribution maps for each pebble. SAM was chosen because this method has been shown by numerous studies to effectively classify lithological and mineral maps from different types of hyperspectral images (Kruse and Lefkoff, 1993; Kruse, 2002; Girouard et al., 2004; Rowan et al., 2005). Moreover, a more practical reason is that it is conveniently included in most image processing software and is relatively easy to implement and interpret contributing greatly to its ease of use.

The classification was undertaken using the different endmembers collected from the images with the output rule images classified through the rule classifier function in ENVI with threshold set at 0.2 radians minimum value for all endmembers. This threshold was chosen to ensure that majority of the pixels are classified and values less than this yield several regions of unclassified pixels. On the other hand, using a higher threshold shows no significant differences in classification results. Mineral identifications from the ASD point measurements were also compared to mineral classification results of the imagery data.

Accuracy assessment of the SAM results was done using manually selected arbitrary points randomly distributed throughout the image. These points are then visually examined and the mineral manually identified based on diagnostic absorption features present. A collection of 30-35 points are collected for each sample and are used as “ground truth” to be input into a confusion matrix to quantify classification accuracy. XRD and thin section results were also used to verify the presence of the minerals identified by spectral methods.

3.2.2. White Mica AlOH Parameters

Several studies have shown than mineralization and degree of metamorphism can be associated to the different types of white mica present in the area (Yang et al., 2001). Thus it is useful to examine the variability of white mica composition within each pebble to get an idea of the range of white mica types present. To achieve this, different parameters where calculated from the AlOH absorption feature which is located at 2200nm wavelength. These parameters are absorption minimum wavelength, absorption depth and crystallinity of white mica. Because the actual minimum wavelength values is highly restricted by the spectral sampling of the instrument and the minimum may fall within the spectral sampling range (10nm) the absorption feature minimum wavelength and depth used were taken by fitting a parabola within the feature and taking the interpolated minimum wavelength and interpolated depth values (Fig. 10). The minimum wavelength position and depth for the 2200nm absorption feature was taken using the spectral range 2150nm-2250nm. Further, crystallinity values are calculated from the ratio of the absorption depth feature at 2200nm to that at 1900nm as shown in Equation 1. The 1900nm OH and water feature parameters were calculated within the spectral range of 1850nm-2130nm. These derived parameters were then calculated for each pixel within an image producing the minimum wavelength, depth and crystallinity images/maps. Processes were implemented using PyENVI software.

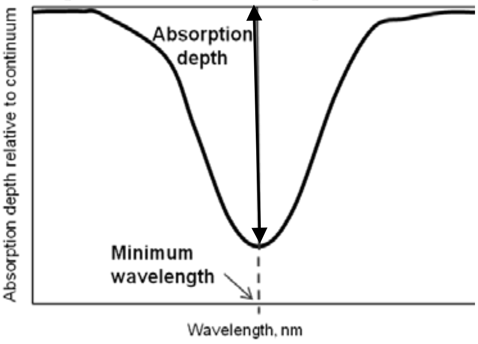

Figure 10. Calculation of absorption depth and wavelength

$$\boxed{\boldsymbol{Crystallinity} = \frac{depth\ of\ AlOH\ absorption\ at\ 2200nm}{depth\ of\ OH + water\ absoprtion\ at\ 1900nm}}$$

Equation 1. Formula for calculating crystallinity of white mica

The derived AlOH parameter maps were then masked to extract regions where white mica has been identified via the SAM classification results. The final images were then used in image analysis in conjunction with the mineral distribution maps and scatter plots of the parameters to distinguish white mica types and alteration textures. Modal values of the AlOH parameters were then determined using the histogram of the images. Peaks in the histogram were considered and these values were plotted in relation to the copper concentration of the samples to find out if there is a relationship between the AlOH parameters to copper enrichment. This was done for the 30 pebbles which have been chemically analyzed.

3.3. Analyses of ASD Point Measurements

ASD measurements from different points in the milled pebble surface were analyzed to identify minerals present in the rock. AlOH parameters including minimum wavelength, absorption depth and crystallinity were also calculated for each ASD white mica spectra. These calculated parameters and mineral identification were then compared to the values determined from the hyperspectral data. Plots of the ASD values against the scatter plot of the image values shows how close the measurements are to each other.

4. RESULTS OF SPECTRAL AND IMAGE ANALYSES

This chapter contains the results of the spectral analyses, both for the ASD point measurements and image endmembers. It discusses the different diagnostic absorption features identified and the variety of minerals found within the milled pebbles for both types of datasets. A discussion of the SAM classification results shows the different mineral distribution within the samples as well as the mineral associations. Results of the analysis of different white mica parameters are also presented as well as the comparison of these image values to values generated from ASD point measurements. The analyses were conducted with the help of ENVI and TSG software.

4.1. ASD Measurements

Several ASD measurements were taken on the split surface of the original 150 milled pebbles set by Mr. Dalm and of this a subset was extracted taking the measurements from the center of the 50 imaged pebbles. However, the following analysis is limited to 32 samples that were chemically analyzed to facilitate correlation of spectral information to copper contents. Descriptions of the diagnostic spectral and absorption features of the different minerals identified in the sample are given below. These results can provide information on the expected minerals that may be encountered as endmembers in the hyperspectral images of the milled pebbles. Original sample numbers were retained from the 150 sample set to avoid confusion.

Several minerals were identified within the samples based on distinct absorption features found in the spectra which were compared to literature and ENVI provided spectral libraries. The minerals encountered are predominantly muscovite and illite. Chlorite and kaolinite were also identified mixed with the two formerly mentioned. The mineral tourmaline was also recognized. Mixtures of muscovite and illite are often collectively referred as white mica/sericite and are used as such in some parts of this thesis (Yang, Huntington et al. 2001; van Ruitenbeek, Cudahy et al. 2005).

Figures 12A and 12B present spectra of white mica contained in the pebbles, muscovite and illite, respectively. For most samples, the wavelength at which the minimum of the 2200nm feature falls within the range 2199.05nm until 2213.97nm. Predominantly the samples (29) are within the 2200-2210nm range which corresponds to average potassic composition white mica (Pontual, Merry et al. 1997). Crystallinity values are generally higher for muscovites compared to illites where the latter have values of less than 2 (Fig. 11 & Eq. 1). The presence of OH overtone bands near 1400nm is clearly identified as well as the H_2O combination absorption feature close to 1900nm (Pontual, Merry et al. 1997; Duke and Lewis 2010). Muscovite is differentiated by the shallower 1900nm water absorption feature compared to the sharper ones found in illites. Depths of these absorption features also vary within the different pebbles. Several studies have linked absorption depths to the mineral abundance present in the sample (van der Meer, 2004). Further, an inflection point at 2160nm in R60, Figure 12B, indicates the presence of kaolinite. One sample in particular, sample 145, have very shallow absorption features and low albedo. Visual inspection confirms the abundance of dark colour minerals in the rock which may significantly lower reflectance and weaken absorption features (Pontual, Merry et al. 1997).

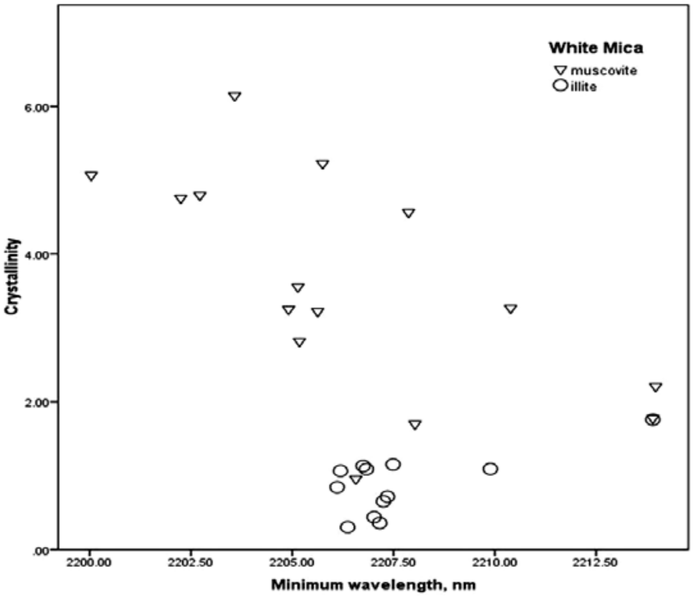

Figure 11. Scatter plot of AlOH minimum wavelength vs. crystallinity

Figure 12C shows the representative spectra of tourmaline and mixtures of tourmaline with muscovite. The bottom green spectrum is pure tourmaline with clear diagnostic features in the 2100-2500nm range, R137. These are series of four absorptions at 2210nm, 2246nm, 2297nm and 2360nm which are attributed to AlOH, MgOH and FeOH vibrations (Clark, 1999). Some workers also suggest that these may be caused by B-OH stretching modes (Hunt, 1977). Strong overtones are also present in the lower wavelengths around 100nm-1500nm because of energy transitions of Fe^{2+} and Fe^{3+} (Clark, 1999). The upper two spectra (red and blue green; R43_1 & R148) correspond to mixtures of tourmaline with muscovite as evidenced by the deeper 2200nm absorption. Furthermore, distinct water and OH absorption in the 1900nm and 1400nm are evident in these spectra which can be attributed to the muscovite component. Figure 12D presents the spectra of mixtures of chlorite with muscovite and illite. The chlorite component is evidenced from the addition of the 2250nm absorption to the typical illite and muscovite spectra shown in Figure 12A and 12B. This additional absorption feature is caused by vibrations in the FeOH bond.

Prior to processing of the hyperspectral images, AlOH parameters of minimum wavelength, depth and crystallinity were calculated from the ASD measurements taken from the center of the milled pebbles. Multiple regression was used to model copper concentration from these AlOH parameters of white mica minerals. Before regression modelling the variables were checked for normality in their distribution using Q-Q plots and Shapiro-Wilk test for normality (Appendix 1). For variables found to be not normal (Fig. 13), values were log transformed to satisfy the normal distribution assumption of the regression modelling. The variables log-transformed are copper concentration, minimum wavelength and crystallinity. Multiple regression modelling was done using the SPSS software. From the 32 ASD spectra, only 30 samples were used because the 2 remaining samples were identified to be tourmaline.

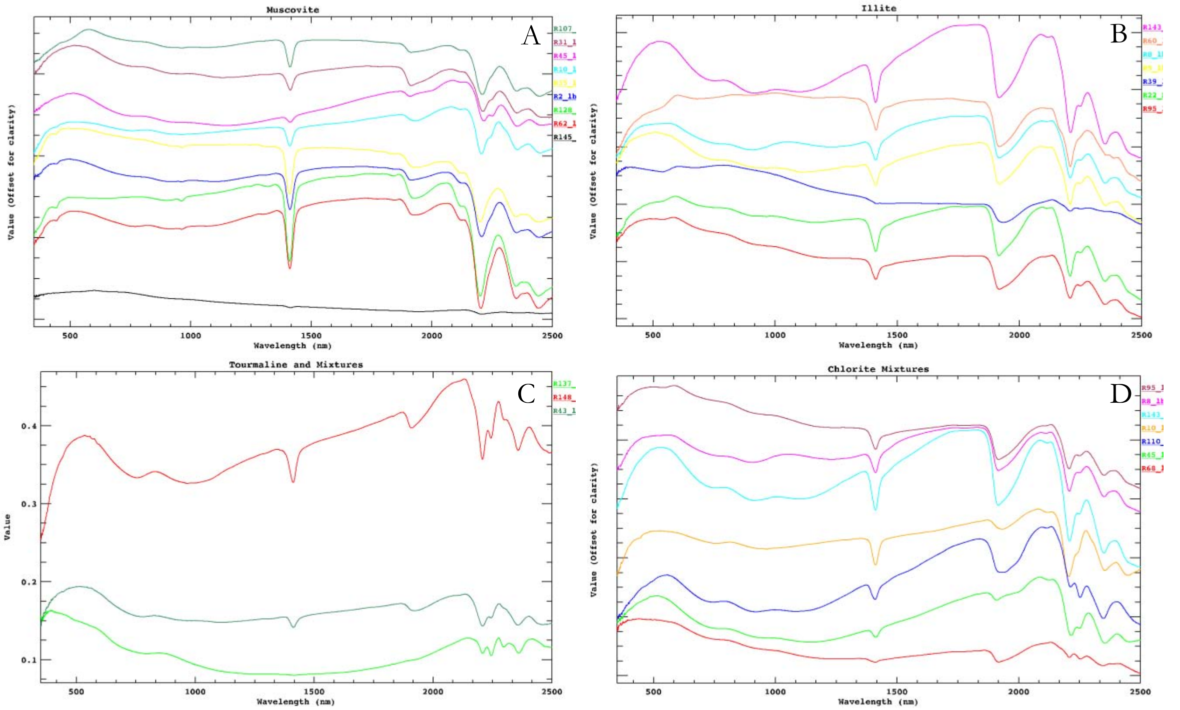

Figure 12. ASD spectra of muscovite(A), illite (B), tourmaline (C) and chlorite (D) together with their mixtures

$$\text{Predicted log Cu} = 467.68 - 0.037(\text{AlOH depth}) - 140(\log \text{AlOH minimum wavelength}) + 0.5(\log \text{crystallinity})$$

Equation 2. Multiple linear regression equation of predicted log Cu content using AlOH depth, minimum wavelength and crystallinity

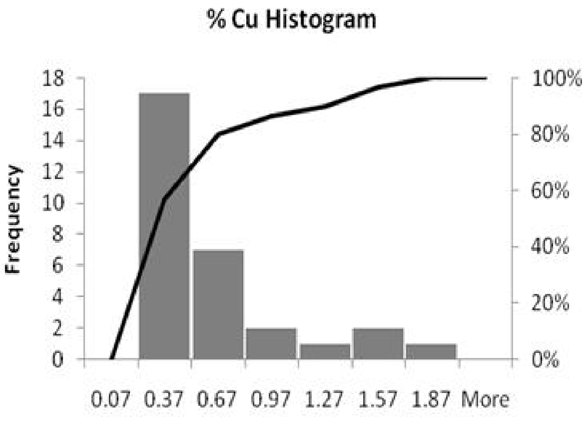

Figure 13. Histogram of copper concentration

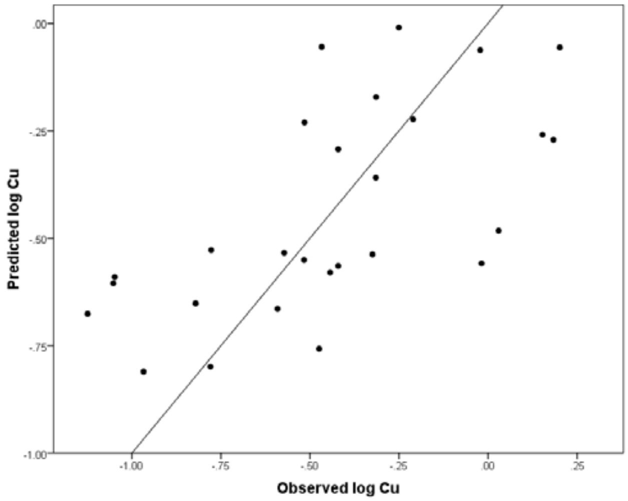

Figure 14. Observed vs. predicted log Cu values from Equation 2

Results of the multiple regression show that only 33% of the observed variance in copper concentration can be accounted by the parameters AlOH depth, minimum wavelength and crystallinity. Equation 2 is the multiple regression equation of the predicted log copper concentration based on the three AlOH parameters. The copper values have negative correlation with depth as well as minimum wavelength and a positive relationship with crystallinity values. However the significance values for depth and minimum wavelength are 0.95 and 0.17, respectively, which are higher than the set alpha of 0.05. Only the crystallinity parameter is significant with a value of 0.01. Standardized coefficients of depth, minimum wavelength and crystallinity are -0.01, -0.24 and 0.50 which indicates that crystallinity has the strongest influence of the predicted copper values compared to the other two parameters. Figure 14 presents the observed log Cu vs. predicted log Cu concentrations which shows that lower values of Cu are overestimated by the model. The results of this analysis show that the relationship between the AlOH parameters calculated from the 30 ASD measurements taken from the center of the milled pebbles cannot be adequately modelled using linear regression.

4.2. Image endmembers

This section presents the minerals that were identified from the hyperspectral imagery and their spectra. It provides a description of the diagnostic absorption features present in the spectra. Identified endmembers were validated based on the results of XRD and thin section analysis.

4.2.1 Spectral characteristics of white mica and their mixtures

Illite and muscovites are the two most predominant minerals present in the milled pebble samples. The spectra of these two minerals which comprise white mica are presented in Figures 15 to 16 as well as the spectra of their mixtures with chlorite and kaolinite. In the first Figure, spectra 5-8 are that of pure illite pixels with distinct absorption feature at 2205nm-2211nm which is due to vibrational absorption of AlOH in their structures (Clark, 1999). Two secondary absorption features due to the same molecule are also found in 2361nm and 2461nm which are shallower than the primary AlOH feature. Another very obvious absorption is found at 1917nm-1936nm which is due to the combination OH stretching and water bending overtones as opposed to fundamental vibrations which are found at longer mid infrared wavelengths (Clark, 1999). At 1415nm another OH overtone is observed which is much narrower than the 1900nm feature. Illite is differentiated from muscovite which have very similar features by its very strong 1900nm OH and water absorption feature. It is also very noticeable that towards the end and start of the spectra there are numerous spikes and the graph appears jagged, this is probably due to sensor noise and does not represent absorption of the minerals present.

The mixtures of illite that were encountered in the milled pebbles are with kaolinite and chlorite. These are represented by the spectra 1-2 and 3-4, respectively, in Figure 15. Kaolinite is identified from the slight inflection at 2166nm. This characteristic absorption is also due to AlOH vibrational processes. For mixtures with chlorite, diagnostic absorption is located at 2255nm and 2342nm which is due to FeOH and MgOH in its chemical structure. Further, a slight dipping of the spectra towards the shorter wavelengths may be due to the presence of ferrous/ferric ions.

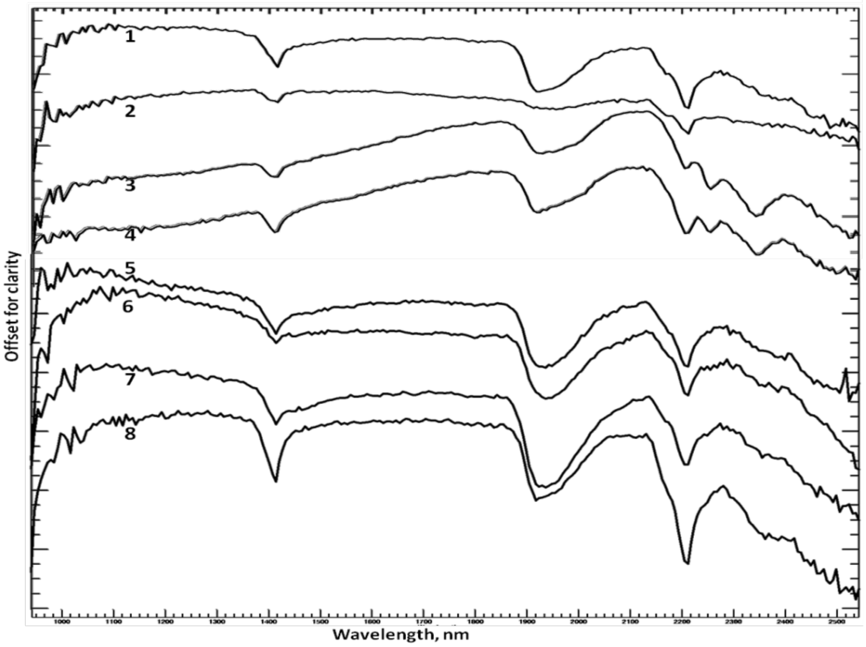

Figure 15. Spectra of Illite and its mixtures (1-2 Illite + Kaolinite; 3-4 Illite + Chlorite; 5-8 Pure Illite)

Figure 16 presents the spectra of muscovite and its mixtures. Similar AlOH features present in the illites are also very conspicuous with the muscovite spectra located at 2205nm-2211nm, 2355nm and 2461nm. Also the 1400nm OH overtone is present. The main difference with illite is found only at the 1900nm absorption feature which is much shallower in the muscovite spectra in relation to the 2205nm absorption. These are shown in spectra 5-9 in the Figure 16.

Mixtures of muscovite with other minerals, tourmaline and chlorite, are shown in spectra 3-4 and 1-2. Tourmaline is identified in the mixture via the 2255nm, 2299nm and 2361nm which is added to the typical muscovite absorptions. These absorptions are due to vibrational processes of FeOH and MgOH components. The mixtures of muscovite and tourmaline can also be differentiated from the pure tourmaline spectra based on the presence of the OH and OH+water absorption features at 1400nm and 1900nm, respectively, which are generally missing in the pure tourmaline. Furthermore, the 2205nm absorption feature is relatively deeper in the mixtures compared to the other features found in the 2200nm-2500nm range.

Muscovite and chlorite mixtures (Fig. 16, spectra 1 & 2) are generally identified from the added absorption at 2255nm, aside from the AlOH, OH and water absorption of muscovites, which is due to the presence of FeOH. Also a much deeper absorption manifests at 2355nm because of the MgOH vibrational processes. Several spectra of this mixture also exhibit a marked dip in the shorter wavelengths due to the presence of Fe^{2+} and/or Fe^{3+}.

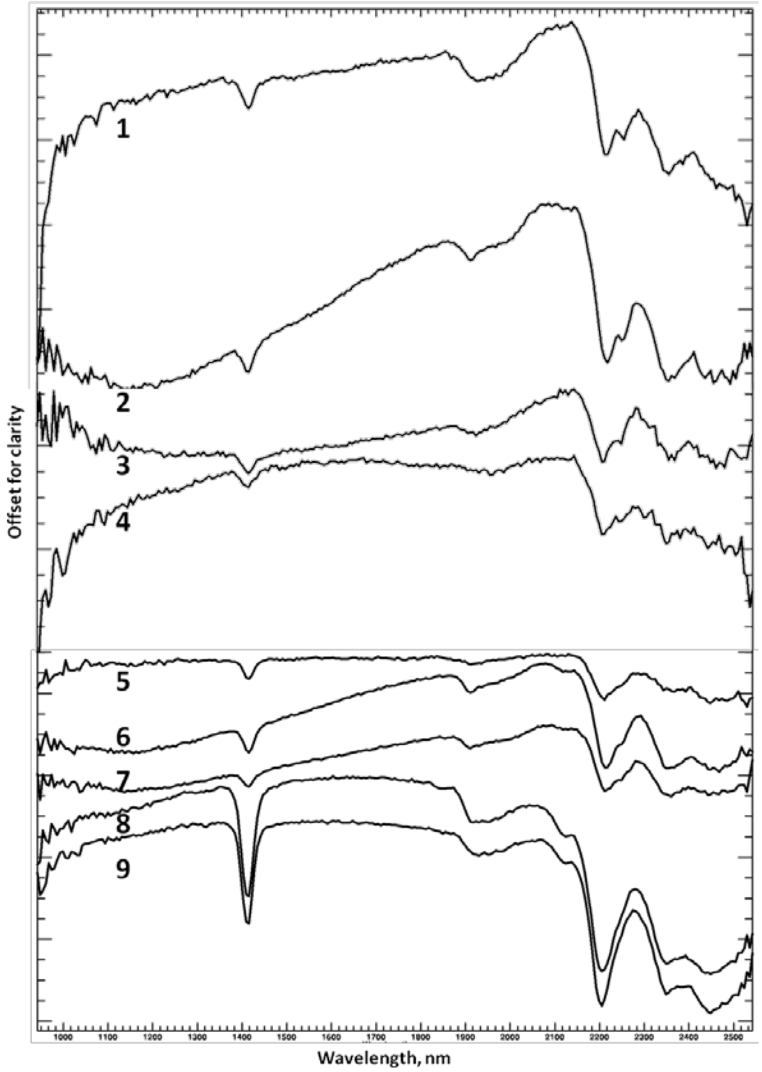

Figure 16. Muscovite spectra and mixtures (1-2 Muscovite+Chlorite; 3-4 Muscovite+Tourmaline; 5-9 Muscovite

4.2.1. Spectral characteristics of tourmaline

The mineral tourmaline is identified within the samples through several absorption features located at 2100nm-2500nm. These are found at 2205nm, 2249nm, 2299nm and 2369nm as shown in Figure 17. These features are attributed to the AlOH, MgOH and FeOH vibrational process although some authors suggests the presence of these features are due to B-OH bending (Hunt, 1977; Clark, 1999). Tourmaline alteration indicates the presence of significant amounts of boron in the circulating hydrothermal fluids (Warnaars et al., 1985; Davidson et al., 2005). Also, compared to the other minerals present in the milled pebbles, tourmalines have significantly lower albedo. Slight dips towards the shorted wavelengths of some spectra may be attributed to the presence of Fe ions.

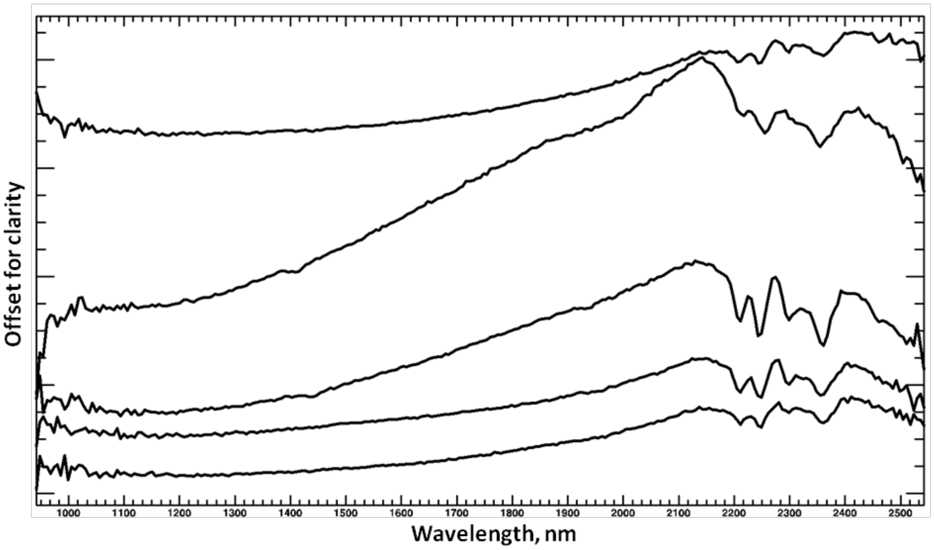

Figure 17. Image endmember spectra of tourmaline

4.2.2. Spectral characteristics of sulphides

Sulphides in the samples are mainly composed of the copper bearing chalcopyrite and pyrite with rare chalcocite. Generally, these minerals are aspectral or do not contain diagnostic absorption features in the SWIR region. However, direct comparison with the spectral image to the rock sample enabled tracing the exact location of the sulphide (chalcopyrite and pyrite) aggregates as the sizes are relatively large with concentrations commonly found along veins. Representative spectra were then extracted based on the locations that were identified.

Figure 18 shows sulphide spectra from the milled pebbles. From this it is apparent that no outstanding absorption features can be detected where random jaggedness of the spectra may be due to sensor noise and not because of the imaged samples. However it was observed that sulphide spectra commonly exhibit low overall reflectance with ranges closer to tourmaline at 20%-10%.

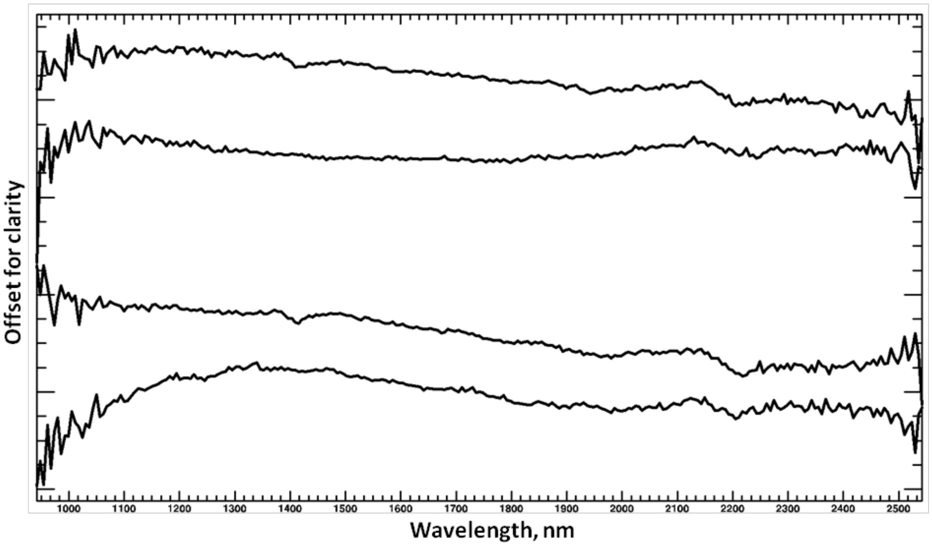

Figure 18. Spectra of sulphides from the hyperspectral images

4.3. Patterns in the spatial distribution of minerals

This section discusses the results of the spectral angle mapper (SAM) classification done using the endmember spectra presented in the previous discussion. SAM classification method was chosen because it is one of the most commonly used method for classification studies and has been proven to work for different types of hyperspectral datasets. Further, this method is easily accessible as it is commonly included in standard image processing software and is relatively easy to implement and interpret.

In this research, different sets of endmembers for every image were used for classification as samples contain different minerals and their mixtures. Thus to optimize accuracy of the classification, endmembers were taken from the images that will be classified. Rule images were then classified using 0.2 radians as threshold because experiments show that values lower than this produce several unclassified regions while values higher than this does not show any significant changes in the classification result.

This section also discusses the results of the analyses done to investigate the white mica present in the milled pebbles in terms of the AlOH minimum wavelength, depth and crystallinity. Images/maps generated by calculating the three AlOH parameters for the whole hyperspectral images were used to examine the patterns of spatial distribution. Scatter plots of the minimum wavelength and crystallinity was also employed to aid in visualizing the range of values of the parameters as well as to examine the relationship with the ASD spectral measurements.

The discussion will be divided per sample and will include the results of the image analyses. These samples were chosen based on their copper content where unmineralized or milled pebbles are included as well as pebbles with increasing copper content. The reason for this was to determine if there is any trend present in the white mica type and their spatial distribution in relation to copper enrichment. In addition, the samples for each range of copper concentration were chosen such that textures that are common in pebbles of that concentration range are represented. These textures include breccias, vein-halo and pervasive/selective alteration.

4.3.1. Sample 45 with 0.087% Cu

Sample 45 is an unmineralized breccia which exhibits vein-halo texture as shown in Figure 19. The numbers in Figure 19-A represent distinct textures where 1-3 are clearly infilled veins as evidenced by their linear orientation and limited extent. A thin darker coloured alteration halo is also apparent on either side of the veins. Towards the middle right of the pebble, Figure 19-A (4), a coarse grained clast is encountered which is also found at the top part of the pebble. This clast can be identified from its coarser grain size in comparison to the gray fine grained matrix.

Figure 19-B shows the results of the SAM classification of the hyperspectral image of sample 45. From this image it can be seen that the identified vein-halo texture (1-3) is composed of tourmaline with the thin darker halo in (1) composed of chlorite+muscovite. Thinner tourmaline veins can also be seen (6) which are oriented perpendicular to the three prominent veins. The fine grained gray matrix is made up of muscovite and chlorite+muscovite mixture. The intimate mixture indicates it has undergone pervasive alteration. The coarse grained clast (4) can be distinguished by the mixture of tourmaline and muscovite however the exact boundary of the clast is difficult to delineate. Close inspection of the SAM image shows that there is a roughly circular occurrence of tourmaline in (5). This is not very clear in the sample photo and may represent relict clast of the breccia that has been intensely altered into muscovite and chlorite. Sulphides are randomly distributed within

this pebble and in some areas show some tourmaline rims. ASD point measurements on the surface of this pebble distinguish only the muscovite+chlorite phase (Table 2). XRD results for this pebble confirms the presence of muscovite and chlorite within the sample (Appendix 2). The presence of muscovite and chlorite suggests that this pebble was sourced from the chlorite sericite alteration zone of the porphyry system.

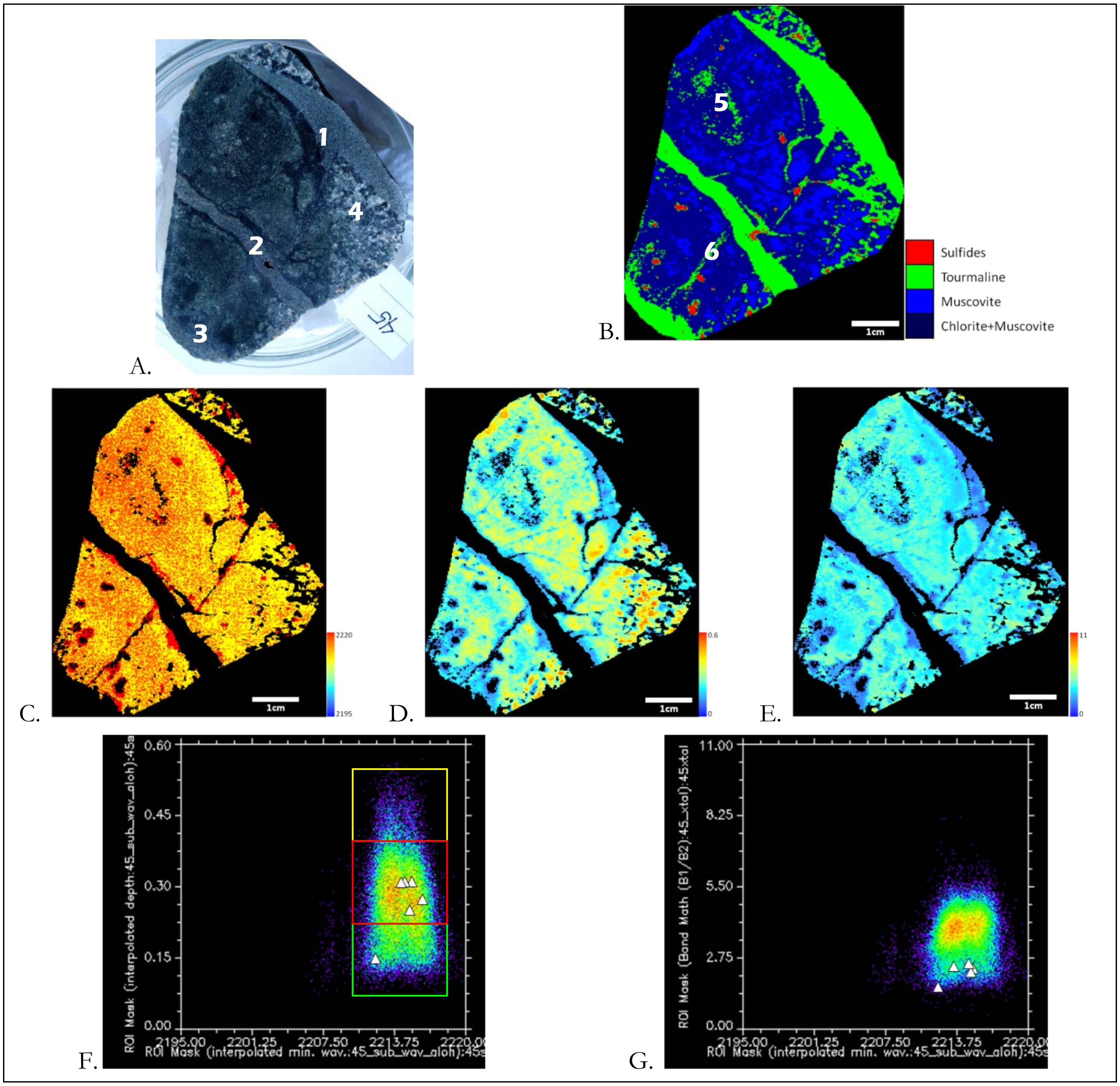

Figure 19. (A) Photograph of sample 45 (numbers are discussed in the text); (B) Mineral map of the sample from SAM classification; (C) Minimum wavelength of AlOH feature at 2200nm map of the sample; (D) Absorption depth map; (E) Crystallinity map; (F) Scatter plot of minimum wavelength of AlOH feature vs. absorption depth. Triangles represent ASD point measurements taken from the same sample. Boxes are explained in the text; (G) Scatter plot of minimum wavelength of AlOH feature vs. Crystallinity. Triangles represent values calculated from ASD point measurements

Figure 19C-E shows the calculated AlOH parameters of the sample which are minimum wavelength of the 2200nm absorption feature, absorption depth and crystallinity, respectively. And Figures 19-F and G shows scatter plots of the minimum wavelength vs. absorption depth (F) and vs. crystallinity (G). The white triangles are the parameters of white mica calculated from the ASD point measurements. The majority of the white mica within this sample have minimum wavelength at 2213nm although values range from 2206nm until 2220nm for the whole image. From Figure 19-C, the longer wavelength white mica are located close to the veins and within the fine grained gray matrix. Comparing these wavelengths to the ASD measurements, the point measurements fall within the range and are close to the modal values calculated from the image (Table 2). In Figure 19-D at least three groups can be identified based on the absorption depth of white mica. Most of the white mica have medium depth at 0.28 (red box in Fig. 19-F) which are mostly composed of the muscovite+chlorite phase and the deepest absorption are found in the pure muscovite areas with most values at 0.38 (yellow box in Figure 19-F). The most shallow white mica absorptions are located close to the veins and halos with modal values of 0.2 (green box in Fig. 19-F). In comparison, most of the ASD measurements fall close to the dominant medium depth range while two measurements (#4 and #5) belong to the shallow absorption depths. Crystallinity of the white mica in this pebble is generally low with values ranging 1.3 to 5.4 with majority falling around 4.0. All of the ASD measurements show relatively significantly lower values than the modal value (4.0) calculated from the hyperspectral imagery.

Table 2. ASD point measurements of Sample 45 and calculated AlOH parameters

Location	**Mineral ID**	**Minimum wavelength @ 2200nm**	**Absorption depth**	**Crystallinity**
1	muscovite+chlorite	2215.57	0.318	2.21
2	muscovite+chlorite	2214.21	0.31	2.12
3	muscovite+chlorite	2213.66	0.26	1.98
4	muscovite+chlorite	2211.94	0.126	0.88
5	muscovite+chlorite	2215.58	0.212	1.68

4.3.2. Sample 22 with 0.17% Cu

Results of the image analyses for Sample 22 are presented in Figures 20-A to G. This sample is coarse grained and appears to have a fairly uniform distribution of grains throughout (Fig. 20-A). The alteration style is mostly texturally retentive with the grain boundaries still discernable indicating selective alteration. In Figure 20-B, classification of the hyperspectral image shows that the pebble is extensively altered to illite and mixtures of illite+chlorite with minor pure chlorite. From this image the illite+chlorite phase commonly appears as discrete patches throughout the image. Based on the boundary characteristics of this illite+chlorite phase which form acute angles, it can be inferred that this material constitute infills. A linear aggregate of the same mineral mixture is also observed at the lower portion of the milled pebble (1) which corresponds to vein mineralization. This linear feature is not clearly seen in the photograph (Fig. 20-A). XRD results for this sample indicate that the main mineral species include chlorite, muscovite, quartz, plagioclase, k-feldspar and rutile. And minerals identified using ASD spectra consist of illite and chlorite mixtures. Mineral assemblage indicates chlorite sericite alteration.

Minimum wavelengths for the main AlOH feature within this pebble range from 2202nm to 22011nm with the majority at 2206nm (Fig. 20-C). In comparison, the minimum wavelengths calculated from the ASD measurements are very close to the modal value of the hyperspectral image, 2206nm-2207nm (Table 3). The distribution of the different wavelengths within the pebble is arbitrary. Figure 20-D shows the absorption depth of the AlOH feature from the hyperspectral data. Modal absorption depth of the image is 0.16 which is close to the ASD point measurements. Looking at the image, areas of deep absorptions are partially or fully surrounded by rims of shallower absorptions which roughly resembles grain boundaries in the pebble. Another linear feature in the upper portion of the pebble (2) indicates vein mineralization that is not clear in the SAM and minimum wavelength image.

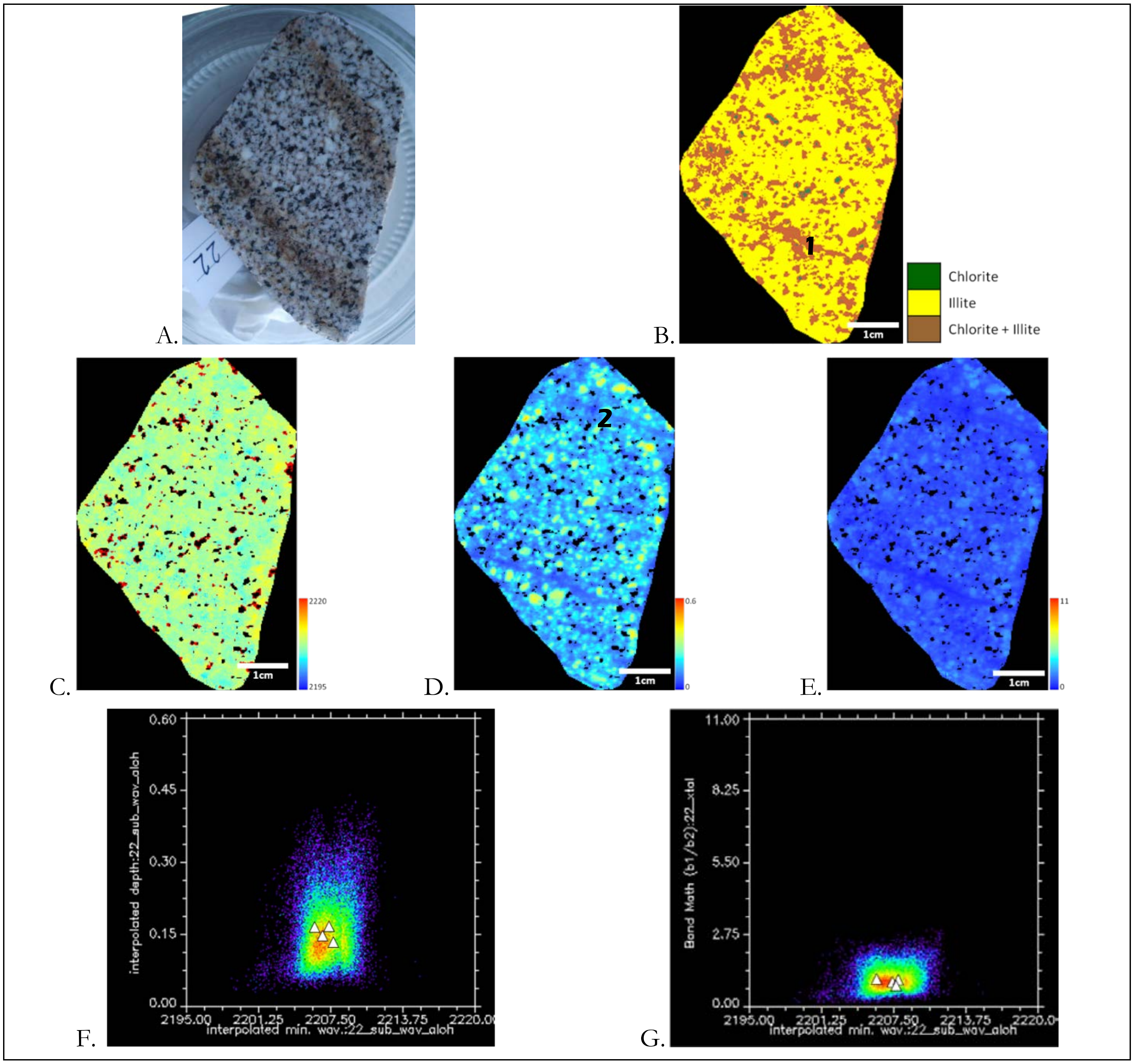

Figure 20. (A) Photograph of sample 22; (B) Mineral map of the sample from SAM classification (numbers are discussed in the text); (C) Minimum wavelength of AlOH feature at 2200nm map of the sample; (D) Absorption depth map; (E) Crystallinity map; (F) Scatter plot of minimum wavlength of AlOH feature vs. absorption depth. Triangles represent ASD point measurements taken from the same sample; (G) Scatter plot of minimum wavlength of AlOH feature vs. Crystallinity. Triangles represent values calculated from ASD point measurements

However in the photograph this appears to be a thin quartz vein which is an aspectral mineral and does not contain diagnostic absorption features in the SWIR. This feature can also be identified in the crystallinity image as a limited linear area with low crystallinity (Fig. 20-E). The crystallinity values calculated from the imagery are generally low with the majority around 0.9 which is comparable to the crystallinity from the ASD point measurements.

Table 3. ASD point measurements for sample 22 and calculated AlOH parameters

Location	Mineral ID	Minimum wavelength at 2200nm	Absorption depth	Crystallinity
1	illite+chlorite	2206.87	0.184	1.06
2	illite+chlorite	2207.27	0.145	0.82
3	illite+chlorite	2207.58	0.167	0.91
4	illite+chlorite	2207.81	0.131	0.70

4.3.3. Sample 137 with 0.23% Cu

Sample 137 is a tourmaline breccias with angular to rounded clasts of altered quartz monzonite (Fig. 21). SAM classification results show that the matrix is composed of tourmaline with disseminated sulphides as shown in Figure 21-B. A thin vein mineralization made up of sulphides is also encountered at the upper portion of the pebble (1). The clasts are pervasively altered to muscovite where the abrupt, as opposed to gradual, change of mineral composition along the boundaries clearly indicates that the clast materials are different from that of the matrix. The mineralogy of the clasts indicates that this pebble have undergone sericite alteration. ASD measurements also identified the two main minerals tourmaline and muscovite in this sample (Table 4). XRD analysis reveals that the sulphides in this pebble are composed of pyrite and other minerals include muscovite as well as quartz.

Figure 21-C presents the minimum wavelength of the AlOH feature for sample 137, from the image, the larger clasts (2) have longer wavelength minimum at around 2211.71nm than those found at the top (3) which are smaller with shorter wavelength minimum, 2207.90nm. The calculated values from the ASD points are closer to the minimum wavelength of the larger clasts with longer wavelengths. In Figure 21-D the smaller clasts at the top (3) have very deep absorptions while the big clasts (2) have relatively shallower depths. The big clasts (2) also have significant variations of absorption depth where shallower depths correspond to the darker areas around the white prismatic muscovite altered crystals. This indicates that muscovite is of less abundance around the darker areas and is mixed with other minerals which may not have diagnostic absorption features in the SWIR. Crystallinity values also vary within the different clasts as shown in Figure 21-E. The mode of the crystallinity values from the hyperspectral data is 5.9 which is greater than the ASD measurements of muscovite while one measurement is quite low because of the effect of tourmaline in the mixture (Table 4).

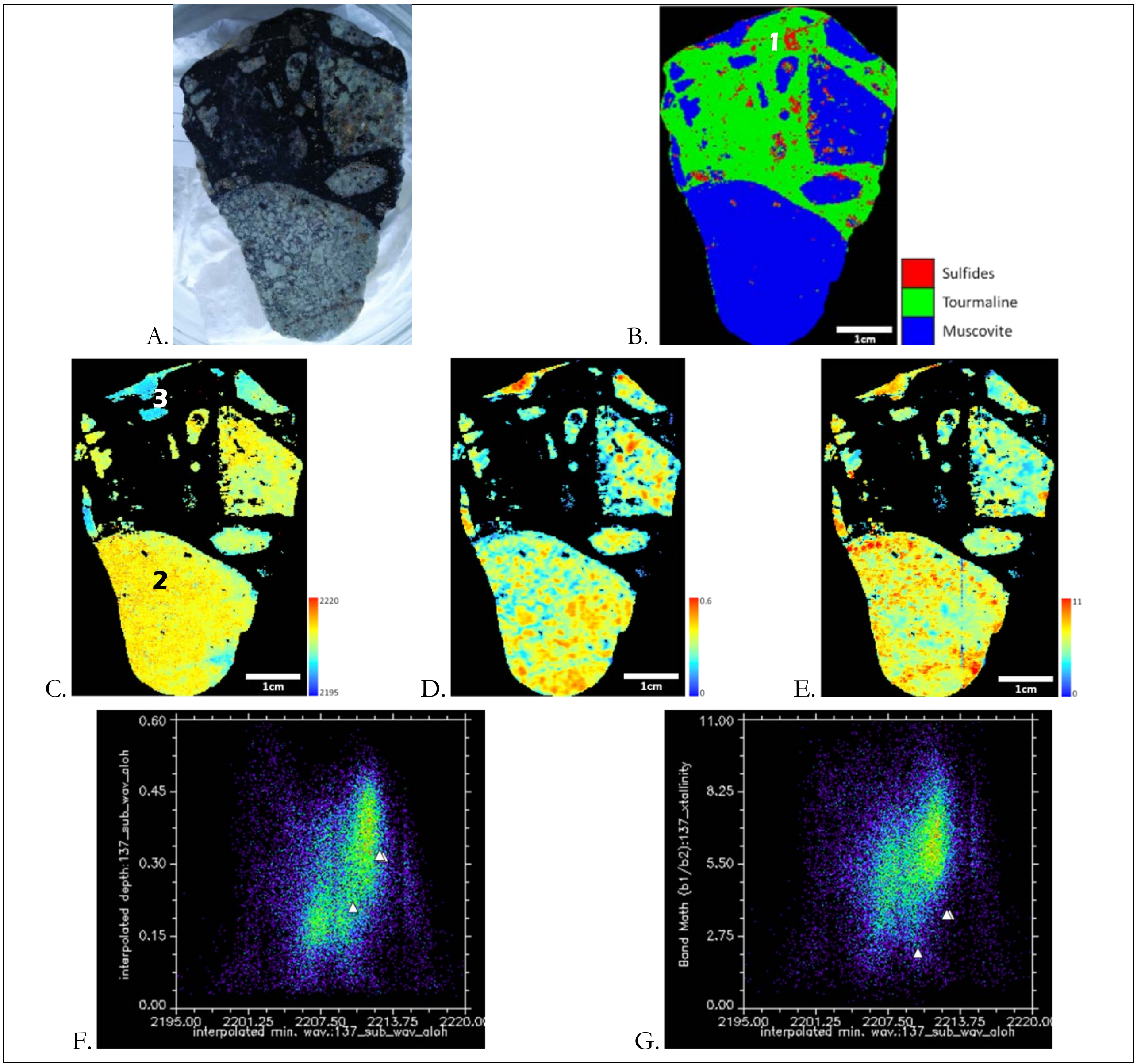

Figure 21. (A) Photograph of sample 137; (B) Mineral map of the sample from SAM classification; (C) Minimum wavelength of AlOH feature at 2200nm map of the sample; (D) Absorption depth map; (E) Crystallinity map; (F) Scatterplot of minimum wavlength of AlOH feature vs. absorption depth. Triangles represent ASD point measurements taken from the same sample; (G) Scatter plot of minimum wavlength of AlOH feature vs. Crystallinity. Triangles represent values calculated from ASD point measurements

Table 4. ASD point measurements for sample 137 and calculated AlOH parameters

Location	Mineral ID	Minimum wavelength at 2200nm	Absorption depth	Crystallinity
1	tourmaline			
2	muscovite	2212.54	0.34	4.97
3	muscovite	2212.73	0.34	4.84
4	muscovite+tourmaline	2210.12	0.21	1.92
5	tourmaline			

4.3.4. Sample 125 with 0.48% Cu

Sample 125 is a mineralized milled pebble that exhibits two different textures, fine grained in the right (1) and coarse grained in the left (2) side as presented in Figure 22-A. However both this sides have been pervasively altered to muscovite based on the results of SAM classification in Figure 22-B. Sulphide occurrences are restricted to the upper left part of the pebble (3) where it is rimmed by tourmaline and mixture of tourmaline+muscovite. All ASD point measurements are identified as muscovite while thin section results confirm the presence of sericite and tourmaline together with pyrite, chalcocite and hematite. Sericite alteration accounts for the dominance of muscovite in the sample.

Minimum wavelength map of the AlOH feature presented in Figure 22-C shows that there is a clear demarcation between shorter wavelengths found in the right (1) which correspond to the fine grained region and the longer wavelengths towards the left (2) composed of the coarse grained area. The shorter wavelengths have modal value of 2201.9nm while the longer wavelength has 2209nm. This trend is also visible in the scatter plot in Figure 22-F where the shorter wavelength species are shown in the red box and the longer wavelength species in the yellow box. This differentiation in wavelength also roughly matches the differences in absorption depths presented in Figure 22-D. Generally the right side (1) shows deeper absorption while the left side (2) has shallower absorption. Transition between these two mica types is gradual and is oriented vertically on the pebble surface. The upper left area (3) close to tourmaline+muscovite mixtures has lower depths. Modal depth of the right (1) region is 0.38 and the left side (2) is 0.42 these values are relatively close to the ASD calculated values (Table 5). Minimum wavelength values from the ASD point measurements are also relatively close to the modal minimum wavelength values taken from the hyperspectral image data. Figure 22-D shows the results of the crystallinity calculated for the image data where the right side (1) has variable crystallinity but with more high values as compared to the left side (2). Majority of the crystallinity values from the hyperspectral imagery is 3.81 which is quite close the ASD derived values.

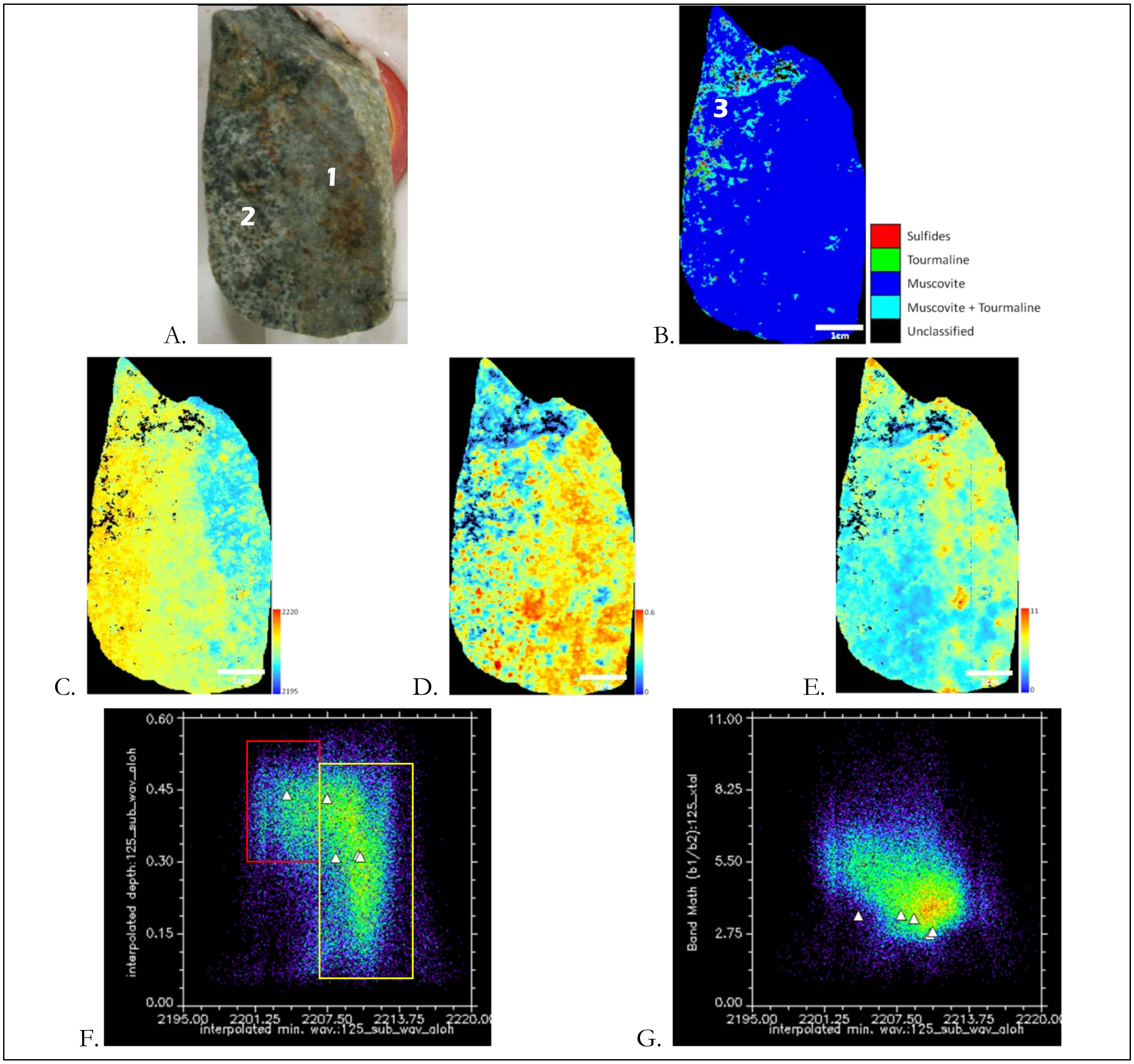

Figure 22. (A) Photograph of sample 125; (B) Mineral map of the sample from SAM classification; (C) Minimum wavelength of AlOH feature at 2200nm map of the sample; (D) Absorption depth map; (E) Crystallinity map; (F) Scatter plot of minimum wavlength of AlOH feature vs. absorption depth. Triangles represent ASD point measurements taken from the same sample. Boxes explained in the text; (G) Scatter plot of minimum wavlength of AlOH feature vs. Crystallinity. Triangles represent values calculated from ASD point measurements

Table 5. ASD point measurements for sample 125 and calculated AlOH parameters

Location	Mineral ID	Minimum wavelength at 2200nm	Absorption depth	Crystallinity
1	muscovite	2209.21	0.39	3.27
2	muscovite	2204.92	0.43	3.62
3	muscovite	2208.21	0.44	3.58
4	muscovite	2210.48	0.33	2.50
5	muscovite	2210.88	0.32	2.90

4.3.5. Sample 60 with 0.96% Cu

This milled pebble sample has relatively high copper content and shows distinct pale brown alteration in (1) and vein-halo in (2). Smaller veins close to (2) with similar orientations are also identified. In the lower right (3) another vein-halo alteration occur perpendicular to (2) and is not as linear in appearance (Fig. 23-A). The classification results show that the vein-halo mineralization is mainly composed of muscovite with minor precipitations of tourmaline and sulphides in the top central region of (2). The smaller vein to the right of (2) is also composed of muscovite as well as the lower right vein (3). Tourmaline and sulphides also occur in (4) and (5). The area in (1) represents pervasively altered host rocks composed of illite and

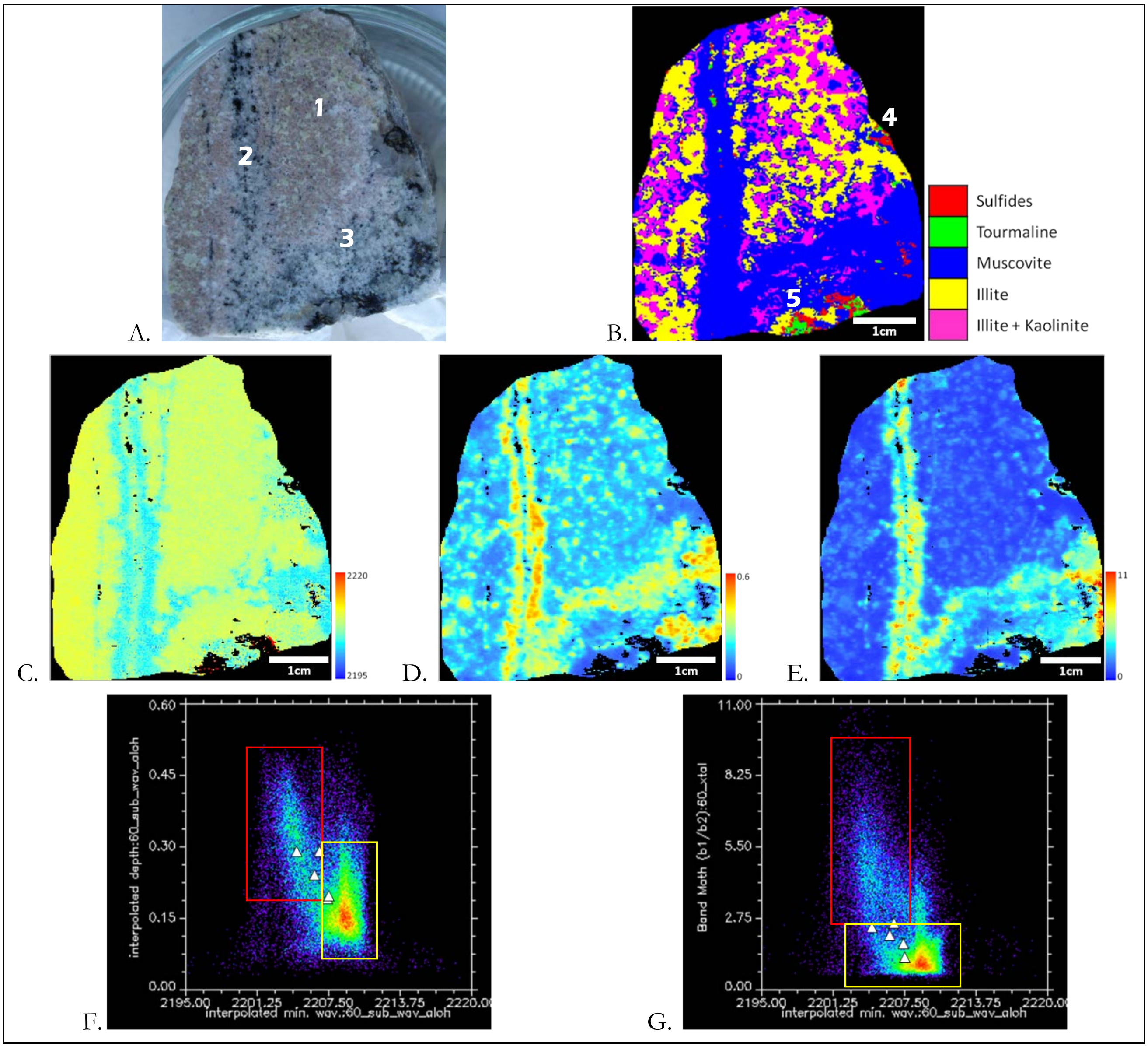

Figure 23. (A) Photograph of sample 60; (B) Mineral map of the sample from SAM classification; (C) Minimum wavelength of AlOH feature at 2200nm map of the sample; (D) Absorption depth map; (E) Crystallinity map; (F) Scatter plot of minimum wavlength of AlOH feature vs. absorption depth. Triangles represent ASD point measurements taken from the same sample. Boxes explained in text; (G) Scatter plot of minimum wavlength of AlOH feature vs. Crystallinity. Triangles represent values calculated from ASD point measurements. Boxes explained in the text.

illite+kaolinite mixture which represents the host rock cut by the stock work veins of muscovite (2 & 3). ASD point measurements identified muscovite and illite within this pebble sample and mixtures of both with kaolinite. XRD analysis shows that minerals present include plagioclase, k-feldspar, quartz, chalcopyrite, chalcocite, rutile and muscovite. The illite + kaolinite mineral assemblage suggests an argillic alteration facies of the host rock which may have been cut or overprinted by sericite alteration stock work veins.

The minimum wavelength map of this pebble found in Figure 23-C shows that the veins are characterized by distinct shorter wavelengths compared to the longer wavelength in region (1). Most of the shorter wavelength found in the veins have values of 2204.5nm while the longer wavelength have values of 2208.9nm. Comparing with the ASD derived minimum wavelength values, one measurement fall within the short wavelength species while the rest are longer but less than the mode of the long wavelength species. Investigation into the different absorption depth of the AlOH feature of white mica in this sample show that the two sides of vein (2) have deep absorption features with a shallow linear central region in between (Fig. 23-D & F). The area in (1) has slightly variable depths. The red box in Figure 23-F covers the short wavelength white mica species with relatively deeper features whereas the yellow box includes the long wavelength species with generally shallower absorption depth. The red box has modal depths of 0.33 while the yellow box has 0.14. The ASD calculated depths fall in between the two modal depth values. Crystallinity values also follow similar patterns of the absorption depth where area (1) has lower crystallinity compared to areas (2) and (3) which are more crystalline. Crystallinity high at (2) and (3) have values commonly reaching 4.4 with a lower crystallinity halo of 1.6 (yellow-high and pale blue-halo in Fig. 23-E). The low crystallinity area in (1) has modal values of 0.98. The ASD derived crystallinity is closer to the value of the pale blue halo found surrounding the muscovite veins in (1) and (2).

Table 6. ASD point measurements for sample 60 and calculated AlOH parameters

Location	**Mineral ID**	**Minimum wavelength at 2200nm**	**Absorption depth**	**Crystallinity**
1	illite+kaolinite	2207.68	0.21	1.15
2	muscovite	2205.76	0.23	1.77
3	illite+kaolinite	2207.64	0.19	1.01
4	muscovite+kaolinite	2206.78	0.29	2.44
5	muscovite	2204.82	0.29	2.29

4.3.6. Sample 43 with 1.04% Cu

Sample 43 is a mineralized tourmaline breccias with matrix composed of black tourmaline (2) and clasts (1) of altered quartz monzonite (Figure 24-A). Mineral map of the pebble produced from classification of hyperspectral data show that disseminated sulphides occur throughout the pebble. Visually it appears that more sulphides are found within the clasts with large aggregates located at region (3). The clasts (1) are made up of intimate mixtures of tourmaline and muscovite indicating pervasive alteration. ASD spectral measurements also identify the two minerals as the main components of this sample. XRD results reveal component minerals include quartz, chalcopyrite, muscovite and tourmaline.

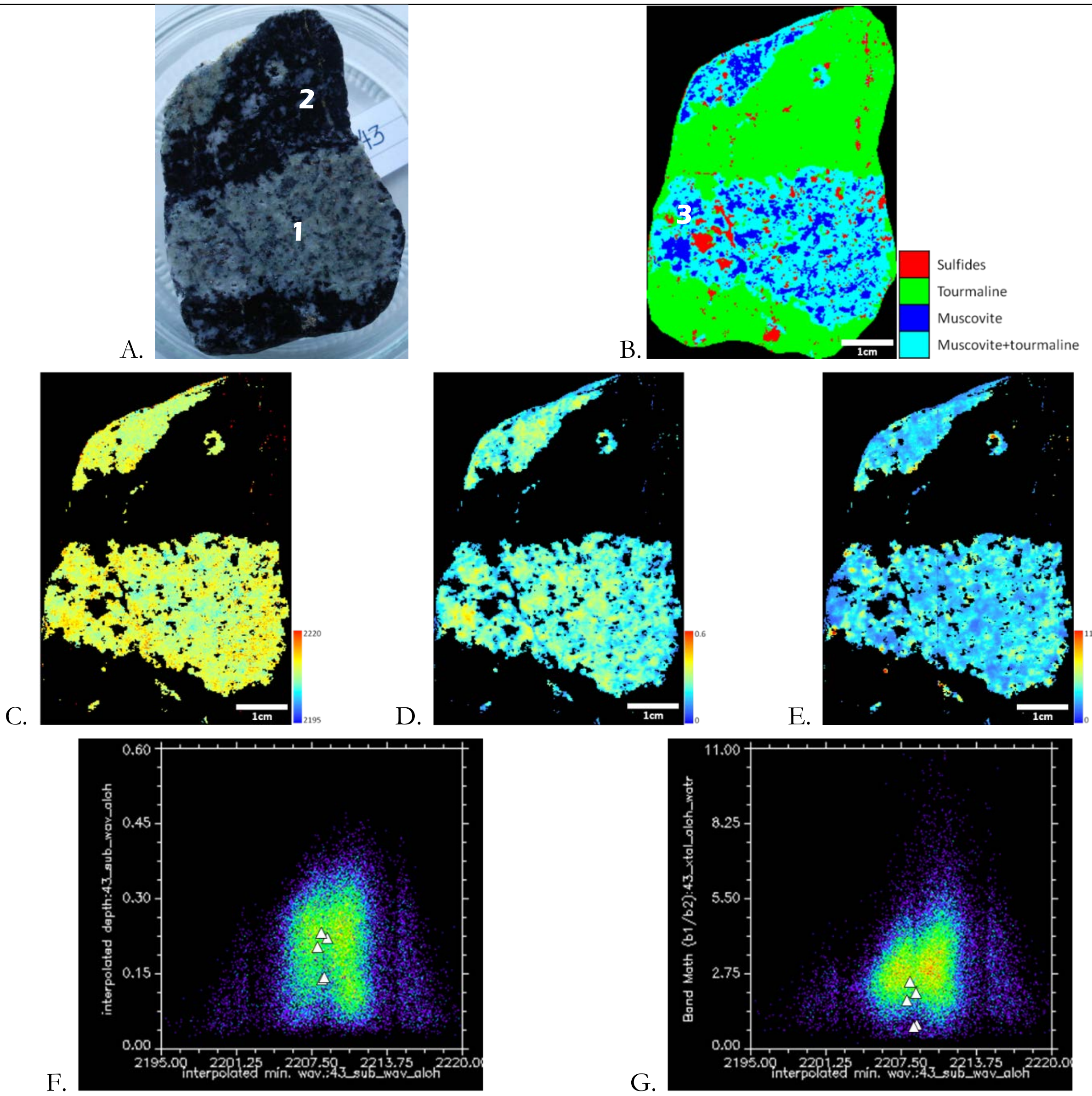

Figure 24. (A) Photograph of sample 43; (B) Mineral map of the sample from SAM classification; (C) Minimum wavelength of AlOH feature at 2200nm map of the sample; (D) Absorption depth map; (E) Crystallinity map; (F) Scatter plot of minimum wavlength of AlOH feature vs. absorption depth. Triangles represent ASD point measurements taken from the same sample; (G) Scatter plot of minimum wavlength of AlOH feature vs. Crystallinity. Triangles represent values calculated from ASD point measurements.

Minimum wavelength of the white mica phases as shown in Figure 24-C have two types, long wavelengths with modal values of 2210.6nm and the short wavelength type with mode of 2217.5nm. Comparing the mineral map with that of the minimum wavelength map reveals that the longer wavelength approximately falls within areas with muscovite+tourmaline mixtures. ASD measurements for minimum wavelength feature are between the two modal values previous mentioned. Absorption depth measurements of the AlOH feature is presented in Figure 24-D which shows that there is also a rough correlation between the deeper absorptions (mode = 0.22) and the occurrence of pure muscovite. Shallower depths are observed where mixtures of muscovite+tourmaline occur with mode equal to 0.11. ASD measurements of two points with muscovite+tourmaline mixture exhibit low absorption depth values while deeper absorption depths are attributed to the muscovite minerals. Relationship with the minerals to that of the crystallinity is not as clear as the other parameters, where modal crystallinity value of the pebble clasts is 2.8 which is higher than the calculated crystallinity values from the ASD measurements.

Table 7. ASD point measurements for sample 43 and calculated AlOH parameters

Location	Mineral ID	Minimum wavelength at 2200nm	Absorption depth	Crystallinity
1	muscovite	2208.2	0.19	1.60
2	muscovite	2209.99	0.20	1.97
3	muscovite+tourmaline	2208.51	0.12	0.85
4	muscovite+tourmaline	2208.86	0.13	0.70
5	muscovite	2208.54	0.24	2.10

4.3.7. Sample 76 with 1.59% Cu

This sample contains the highest copper concentration in the set of milled pebbles that have been chemically analyzed. It contains several cross cutting veins within a pervasively altered host rock (Figure 25-A). Classification results show that the thin linear veins (1) are composed of tourmaline with sulphide mineralization (Fig. 25-B). Towards the left part of the pebble (2) abrupt linear boundary of the occurrences of tourmaline and sulphide signify possible vein-halo alteration in this region. The rest of the pebble is composed of muscovite which is a product of pervasive alteration. Only muscovite has been identified using the ASD point measurements while XRD results show constituent minerals include quartz, muscovite and pyrite. The lack of tourmaline in the XRD results may be due to the sporadic distribution of the mineral and it is possible that the sample used for the analysis may not contain significant tourmaline. Abundance of muscovite implies sericite alteration facies.

Minimum wavelength map of this pebble shown in Figure 25-C illustrates that most of the white mica present have short minimum wavelength with values mostly at 2201nm. This is comparable with the minimum wavelength calculated from the ASD points. Closer inspection of the minimum wavelength map show that a halo can be identified enveloping the tourmaline veins in (3) and (4). This textural feature can be identified by the slightly longer minimum wavelength compared to the background value. Absorption depths of the AlOH feature are quite deep with modal value of 0.46 which is close to two ASD spectra values. The three other ASD measurements have shallower absorption depths. Crystallinity is high towards the left side of the pebble (2) close to the occurrences of tourmaline and sulphides. This region has modal crystallinity value of 8.4 while the rest of the pebble has 5.11. Values for crystallinity calculated from the ASD points are all lower than the modal value taken from the hyperspectral image data.

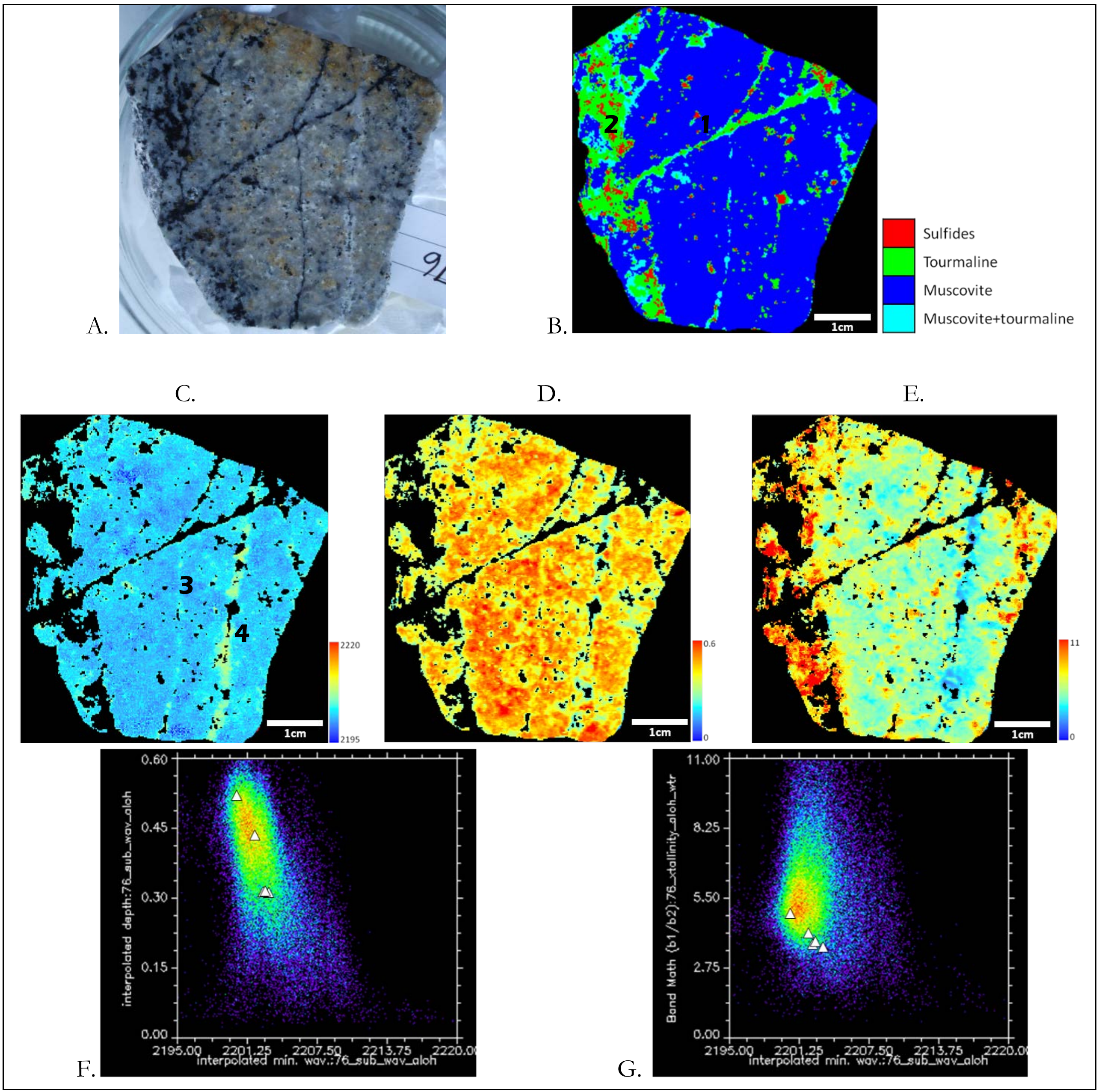

Figure 25. (A) Photograph of sample 76; (B) Mineral map of the sample from SAM classification; (C) Minimum wavelength of AlOH feature at 2200nm map of the sample; (D) Absorption depth map; (E) Crystallinity map; (F) Scatter plot of minimum wavlength of AlOH feature vs. absorption depth. Triangles represent ASD point measurements taken from the same sample; (G) Scatter plot of minimum wavlength of AlOH feature vs. Crystallinity. Triangles represent values calculated from ASD point measurements.

Table 8. ASD point measurements for sample 76 and calculated AlOH parameters

Location	Mineral ID	Minimum wavelength at 2200nm	Absorption depth	Crystallinity
1	muscovite	2200.95	0.52	4.80
2	muscovite	2202.03	0.38	4.00
3	muscovite	2202.78	0.38	3.95
4	muscovite	2203.22	0.37	3.48
5	muscovite	2202.02	0.43	3.92

4.4. Types of white mica in copper enriched milled pebbles

In order to determine the different types of white mica, as characterized by the AlOH parameters, present in the milled pebbles with high copper concentrations, modal values of the three calculated parameters are determined from the AlOH parameter (crystallinity, minimum wavelength and absorption depth) images. Several milled pebble images exhibit more than one mode which appears as multiple peaks in the image histograms. To account for the different species of white mica, the values of the different peaks were included in the analysis.

Figure 26 shows the crystallinity values of 30 milled porphyry copper pebbles ordered in decreasing copper contents. Dashed line indicates the cut-off grade of 0.4% Cu. Based on the distribution of the crystallinity values, it can be deduced that most milled pebbles with high copper content contain white micas that are relatively more crystalline than those found in pebbles which are unmineralized or with low copper values. Crystallinity values for milled pebbles above the cut-off grade are generally higher than 0.33 although some white mica species also co-occur which are of lesser crystallinity as seen in samples 148, 60, 62 and 31. Pebbles below the cut-off grade usually have crystallinity values of less than 0.2. High crystallinity values are obtained until sample 97, dotted line, which contain 0.3% copper. Copper concentration appears to be related to higher crystallinity values although the relationship is not very straight forward.

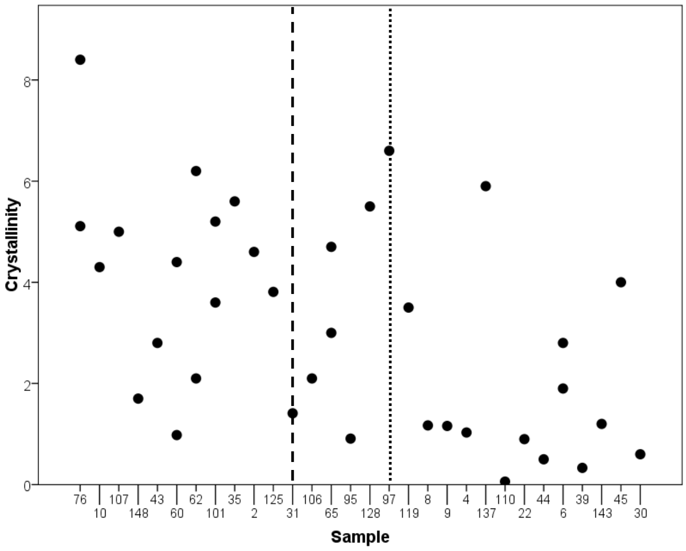

Figure 26. Modal crystallinity values from images of milled porphyry copper pebbles. (Sample numbers are ordered in decreasing Cu content. Lines discussed in text.)

Figure 27 shows the modal minimum wavelength values of the milled pebbles samples. From this figure, it can be seen that pebbles with less than 0.3% Cu (dotted line) do not have white mica species with short wavelengths compared to those with higher concentrations. Most of the high grade milled pebbles contain white mica types with minimum wavelengths of less than 2206nm. Longer wavelengths also co-exist within the same pebbles. From these results, it can be deduced that copper mineralization is related to the short wavelength white micas.

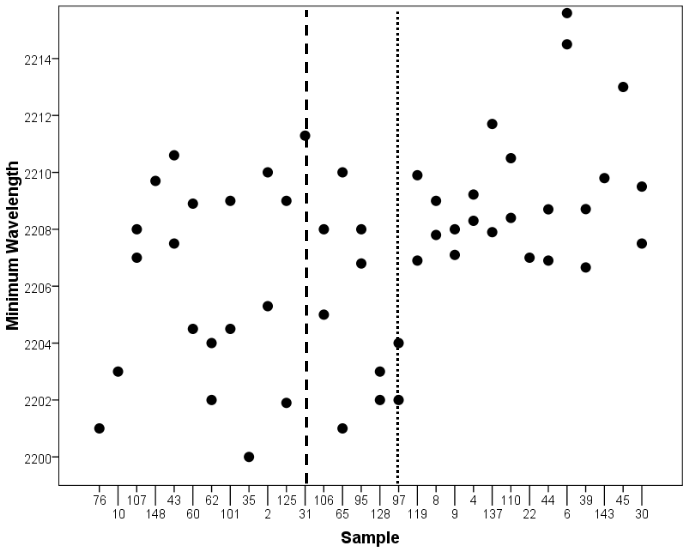

Figure 27. Modal minimum wavelengths of the AlOH absorption feature from images of milled porphyry copper pebbles. (Sample numbers are ordered in decreasing Cu content. Lines discussed in text.)

Figure 28 shows the different modal absorption depths of the copper milled pebbles. Based on this graph, pebbles above the cut-off grade contain deep absorption features while unmineralized pebbles have shallower absorption features especially for pebbles with less than 0.3% Cu (dotted line). White mica with shallow absorption features also coexist with the deep absorption white mica in some of the high grade porphyry milled pebbles. Low grade milled pebbles generally have absorption depth less than 0.3.

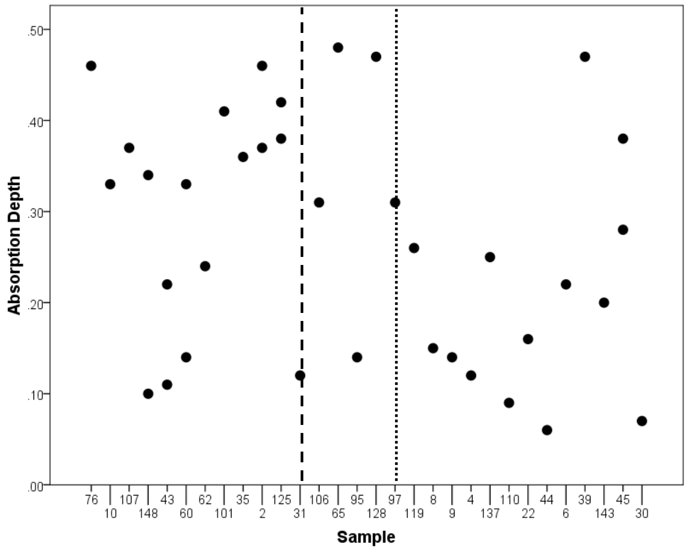

Figure 28. Modal absorption depths of the AlOH absorption feature from images of milled porphyry copper pebbles. (Sample numbers are ordered in decreasing Cu content. Lines discussed in text.)

4.5. Summary

In this chapter, results of the different analyses were presented starting with the ASD point measurements where several minerals were identified including tourmaline, white mica (illite and muscovite), kaolinite, and chlorite. These minerals were also determined from the spectra extracted from the hyperspectral images of the milled pebbles with the addition of sulphides. Examination of the different mineral distribution show that several alteration textures such as veins can be delineated based on the extent of infill and/or alteration mineral. The nature of the mixtures of the different end members in the minerals maps also provides clues to the kind of alteration that is present like pervasive and selective alteration in sample 76 and 22, respectively. Comparisons with the minerals identified by the ASD point measurements show that some mineral species may not be identified by ASD measurements probably because of the limited spatial extent of the occurrences. Minerals identified by the spectral methods were confirmed by the XRD and thin section analyses.

Analyses of the AlOH parameter maps of the different milled pebbles show that changes in the alteration characteristics are reflected as changes in minimum wavelength, crystallinity and depths of the absorption features. Several vein-halo alterations were identified because of the different wavelength minimum within and around the vein compared to background values represented by majority of the rock surface. This characteristic is well illustrated in sample 76 and 60. Comparison of the AlOH parameters calculated from ASD point measurements to parameters from the image data show that values from the former commonly falls within the range of values from the latter dataset. However, the values obtained from the ASD points frequently do not fall within the modal value of the imagery data. Only when the sample is relatively homogenous like sample 22 does the ASD measurement fall close to the modal values of the imagery. This is because the ASD point measurements have a relatively larger sampling area, compared to the imagery, and values obtained are somewhat averaged for that area. This difference also arises with minerals that occur in limited areas in the pebble which are not identified by the ASD point measurements. Graphing the different AlOH parameters of the 30 milled pebbles, that were chemically analyzed, shows that pebbles with higher copper concentration contain white mica species with shorter minimum wavelength, high crystallinity values and deep absorption features.

5. CONCLUSIONS

Based on the results of the analyses done the following are concluded:

- Diagnostic spectral absorption features of alteration minerals in the SWIR region are clearly identifiable with the SisuCHEMA-acquired high resolution hyperspectral data. And minerals predominant in the milled pebble samples identified based on their spectral characteristics include white mica (muscovite and illite), tourmaline, sulphide minerals, and mixtures with chlorite and kaolinite.

- Mineral distribution maps generated provide detailed information of the spatial distribution of the different minerals, both alteration and ore. The mineral distribution patterns such as linearity, limited extent and nature of the mixture of different mineral phases provide clues to the type of alteration texture present such as vein-halo, pervasive or selective alteration.

- The minimum wavelength of white mica present in the pebbles range from 2197nm until 2217nm but the modal wavelengths fall within 2202nm until 2213nm which indicates normal potassic white mica composition.

- The different AlOH parameters, minimum wavelength, absorption depth and crystallinity, are able to differentiate textures in the image including vein-halo, pervasive and selective alteration based on their spatial distribution and variation.

- Based on visual examination, image textures on the AlOH parameter maps correspond to real geologic textures present in the surface of the milled pebbles samples.

- Comparing the different AlOH parameters calculated from the hyperspectral imagery and the ASD measurements show that ASD derived parameters fall within the range of values from the imagery. However, frequently the ASD values do not coincide with the modal values from the hyperspectral images.

- Copper enrichment is related to high crystallinity, short AlOH minimum wavelength and deep absorption white mica types

- Hyperspectral imagery data provides several advantages over point data measurements like:
    - It allows examination of the entire range of white mica types present in the pebble and their spatial distribution patterns
    - Determination of the dominant white mica species is possible
    - Occurrences of minor minerals present can be identified which may be missed by point measurements
    - Delineation of textural regions such as vein-halo alteration, pervasive and selective alteration is possible

6. RECOMMENDATIONS

Further studies should be conducted to investigate the ability of this type of hyperspectral images to distinguish textural information. Possible methods that can be used to characterize textures include edge maps of the original hyperspectral data as well as the derived AlOH parameter maps. This will provide information on the local variability of the dataset. Such variability in the AlOH parameter has been shown to indicate changes in geologic texture.

LIST OF REFERENCES

Bateman, A.M., 1955, Economic mineral deposits, John Wiley & Sons, Inc., 604 p.

Bierwirth, P.N., 2004, Laboratory and imaging spectroscopy of tourmaline - A tool for mineral exploration, Volume 2010.

Brown, A.J., Cudahy, T.J., and Walter, M.R., 2006, Hydrothermal alteration at the Panorama Formation, North Pole Dome, Pilbara Craton, Western Australia: Precambrian Research, v. 151, p. 211-223.

Chen, X., Warner, T.A., and Campagna, D.J., 2007, Integrating visible, near-infrared and short-wave infrared hyperspectral and multispectral thermal imagery for geological mapping at Cuprite, Nevada: Remote Sensing of Environment, v. 110, p. 344-356.

Clark, R.N., 1999, Chapter 1:Spectroscopy of Rocks and Minerals, and Principles of Spectroscopy, *in* Rencz, A.N., ed., Manual of Remote Sensing, Volume 3: Remote Sensing for the Earth Sciences: New York, John Wiley and Sons, p. 3-58.

Cloutis, 1996, Hyperspectral geological remote sensing: evaluation of analytical techniques: International Journal of Remote Sensing, v. 17, p. 2215-2242.

Cudahy, T.J., Wilson, J., Hewson, R., Okada, K., Linton, P., Harris, P., Sears, M., and Hackwell, J.A., 2001, Mapping porphyry-skarn alteration at Yerington, Nevada using airborne hyperspectral VNIR-SWIR-TIR imaging data, Geoscience and Remote Sensing Symposium. IGARSS '01. IEEE 2001 International Volume 2: Sydney, NSW, Australia p. 631-633.

Davidson, P., Kamenetsky, V., Cooke, D., Frikken, P.H., Hollings, P., Ryan, C., Achterbergh, E.V., Mernagh, T., Skarmeta, J., Serrano, L., and Vargas, R., 2005, Magmatic precursors of hydrothermal fluids at the Rio Blanco Cu-Mo deposit, Chila: Links to silicate magmas and metal transport: Economic Geology, v. 100, p. 963-978.

Duke, F.E., 1994, Near infrared spectra of muscovite, Tschermak substitution, and metamorphic reaction progress: Implications for remote sensing: Geology, v. 22, p. 621-624.

Duke, F.E., and Lewis, R.S., 2010, Near infrared spectra of white mica in the Belt Supergroup and implications for metamorphism: American Mineralogist, v. 95, p. 908-920.

Gifkins, C., Herrmann, W., and Large, R., 2005, Altered volcanic rocks: A guide to description and interpretation: Tasmania, Australia, Center for Ore Deposit Research, 275 p.

Girouard, G., Bannari, A., Eli Harti, A., and Desrochers, A., 2004, Validated Spectral Angle Mapper Algorithm for Geological Mapping: Comparative Study Between Quickbird and Landsat-TM, XXth ISPRS Congress: Istanbul, Turkey, p. 599.

Guilbert, J.M., and Park, C.F., 1986, Geology of ore deposits: New York, W. H. Freeman and Company, 405-426 p.

Hermann, W., Blake, M., Doyle, M., Huston, D., Kampard, J., Merry, N., and Pontual, S., 2001, Short wavelength infrared (SWIR) spectral analysis of hydrothermal alteration zones associated with base metal sulfide deposits at Roseberry and Western Tharsis, Tasmani and Highway-Reward, Queensland: Economic Geology, v. 96, p. 939-955.

Hestir, E.L., Khanna, S., Andrew, M., Santos, M., Viers, J., Greenberg, J., Rajapakshe, S., and Ustin, S., 2008, Indentification of invasive vegetation using hyperpsectral remote sensing in California Delta ecosystem: Remote Sensing of Environment, v. 112, p. 4034-4047.

Hunt, G.R., 1977, Spectral Signatures of particulate minerals in the visible and near infrared: Geophysics, v. 42, p. 501-513.

Hunt, G.R., and Ashley, R.P., 1979, Spectra of altered rocks in the visible and near infrared: Economic Geology, v. 74, p. 1613-1629.

Huntington, J.F., Mauger, A.J., Skirrow, R., Bastrakov, E., Connor, P., Mason, P., Keeling, J., Coward, D., Berman, M., Philipps, R., Whitbourn, L., and Heithersay, P., 2004, Automated mineralogical logging of core from the Emmie Bluff iron oxide copper-gold prospect, South Australia, PACRIM Congress: Adelaide, South Australia, AUSIMM.

Huntington, J.F., Whitbourn, L., Mason, P., Berman, M., and Schodlok, M.C., 2011, HyLogging-Voluminous industrial-scale reflectance spectroscopu of the earth's subsurface, Volume 2011.

Kruse, F.A., 1998, Advances in hyperspectral remote sensing for geologic mapping ang exploration, 9th Australian Remote Sensing Conference: Sydney, Australia.

Kruse, F.A., 2002, Comparison of AVIRIS and Hyperion for Hyperspectral Mineral Mapping, 11th JPL Airborne Geoscience Workshop: Pasadena, California.

Kruse, F.A., and Lefkoff, A.B., 1993, Knowledge-based geologic mapping with imaging spectrometers: Remote Sensing Reviews, v. 8, p. 3-28.

Kurniawan, A., McKenzie, J., and Putri, J.A., 2009, General dictionary of geology: Yogyakarta, Indonesia, Environmental Geographic Student Association.

Mauger, A.J., and Hore, S., 2009, Integrating mineralogical interpretation of Hylogger data with Hymap mineral mapping, Mount Painter, South Australia, *in* Jones, S., and Reinke, K., eds., Innovations in remote sensing and photogrammetry, Lecture notes in geoinformation and cartography: Berlin Heidelberg, Springer-Verlag, p. 271-280.

McMillan, W.J., and Panteleyev, A., 1980, Ore deposit models-1.Porphyry Copper Deposits: Geoscience Canada, v. 7, p. 52-63.

Meunier, A., and Velde, B., 2004, Illite:Origins, evolution and metamorphism, Springer, 286 p.

Pirajno, F., 2009, Hydrothermal processes and mineral systems: Australia, Springer.

Pontual, S., Merry, N., and Gamson, P., 1997a, G-MEX - Porphyry Alteration Systems, AusSpec International Pty. Ltd.

Pontual, S., Merry, N., and Gamson, P., 1997b, G-MEX - Spectral Interpretation Field Manual, AusSpec International Pty. Ltd., 153 p.

Rajesh, H.M., 2004, Application of remote sensing and GIS in mineral resource mapping - An overview: Journal of Mineralogical and Petrological Sciences, v. 99, p. 83-103.

Rowan, L.C., MArs, J.C., and Simpson, C.J., 2005, Lithologic mapping of Mordor, NT, Australia ultramafic complex by using ASTER: Remote Sensing of Environment, v. 99, p. 105-126.

Sabins, F.F., 1999, Remote sensing for mineral exploration: Ore Geology Reviews v. 14, p. 157–183.

Sillitoe, R.H., 2010, Poprhyry copper systems: Economic Geology, v. 105, p. 3-41.

South, S., Qi, J., and Lusch, D., 2004, Optimal classification methods for mapping agricultural tillage practices: Remote Sensing of Environment, v. 91, p. 90-97.

Spectral Imaging Ltd., 2007, SisuCHEMA, Volume 2010.

Taylor, R.G., 2009, Ore Textures: Recognition and Interpretation: Berlin, Springer-Verlag.

United States Geological Survey, 2010, Copper:Mineral commodity summaries, Volume 2010.

van der Meer, F.D., 2004, Analysis of spectral absoprtion features in hyperspectral imagery: International Journal of Applied Earth Observation and Geoinformation, v. 5, p. 55-68.

van der Meer, F.D., and de Jong, S.M., 2001, Imaging Spectrometry: Basic Principles and Prospective Applications: Dordrecht, The Netherlands, Springer, p. 403.

van Ruitenbeek, F.J.A., Cudahy, T.J., Hale, M., and van der Meer, F.D., 2005, Tracing fluid pathways in fossil hydrothermal systems with near-infrared spectroscopy: Geology, v. 33, p. 597-600.

van Ruitenbeek, F.J.A., Debba, P., van der Meer, F.D., Cudahy, T.J., van der Meijde, M., and Hale, M., 2006, Mapping white micas and their absorption wavelengths using hyperspectral band ratios: Remote sensing of Environment, v. 102, p. 211-222.

Warnaars, F.W., Holmgren, D.C., and Barassi, F.S., 1985, Pophyry copper and tourmaline breccias at Los Bronces-Rio Blanco, Chile: Economic Geology, v. 80, p. 1544-1565.

Yang, K., Huntington, J.F., Browne, P.R.L., and Ma, C., 2000, An infrared spectral reflectance study of hydrothermal alteration minerals from the Te Mihi sector of the Wairakei geothermal system, New Zealand: Geothermics, v. 29, p. 377-392.

Yang, K., Huntington, J.F., Cudahy, T.J., Mason, P., and Scott, K.M., 2001, Spectrally mapping the compositional variation of white micas in hydrothermal systems and the application in mineral exploration, Geoscience and Remote Sensing Symposium. IGARSS '01. IEEE 2001 International Volume 7: Sydney, NSW , Australia, p. 3294-3296.

APPENDICES

Appendix 1. Histogram and normality tests of ASD measurements used for multiples regression analysis

Shapiro-Wilk Test for Normality

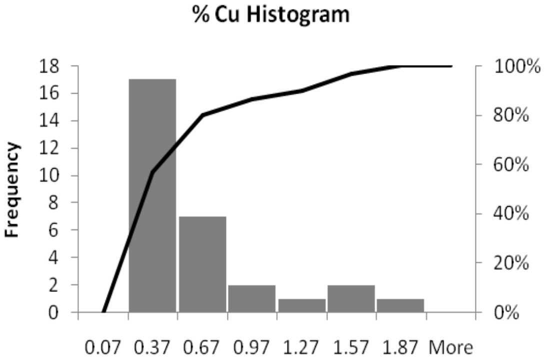
% Cu Histogram

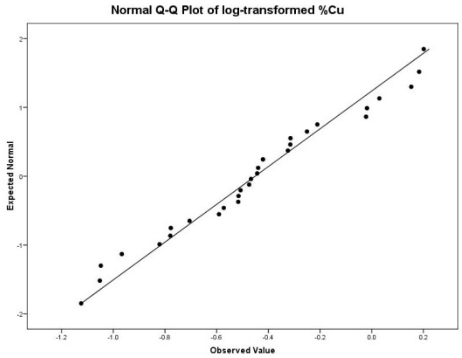
Normal Q-Q Plot of log-transformed %Cu

0.413

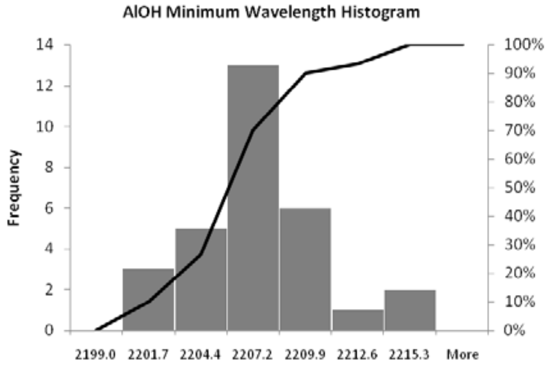
AlOH Minimum Wavelength Histogram

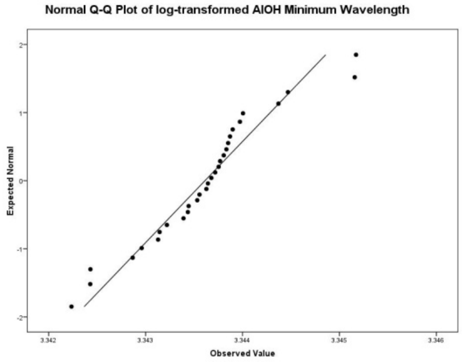
Normal Q-Q Plot of log-transformed AlOH Minimum Wavelength

0.155

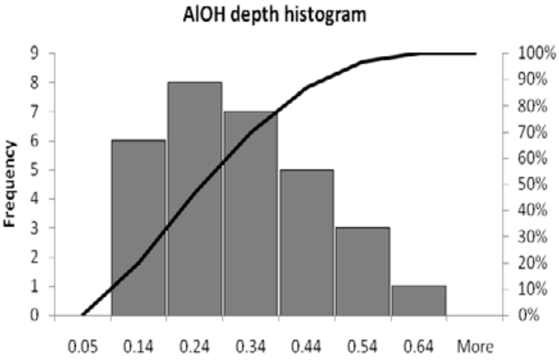
AlOH depth histogram

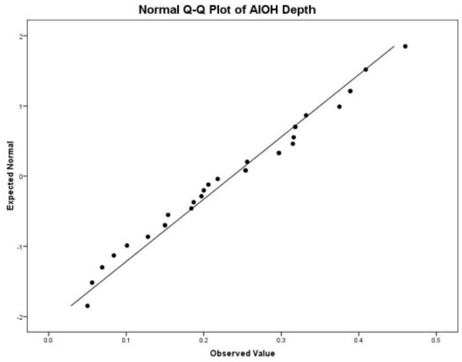
Normal Q-Q Plot of AlOH Depth

0.542

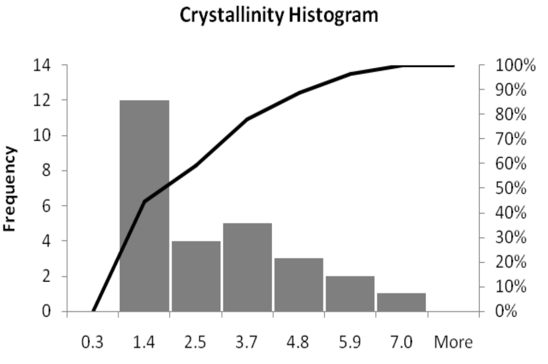
Crystallinity Histogram

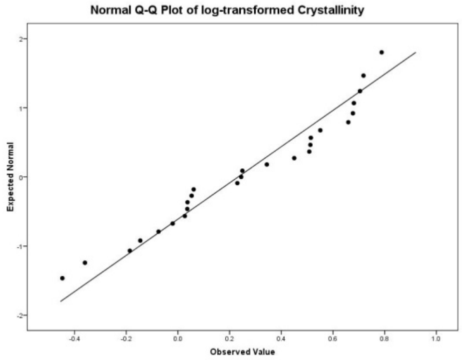
Normal Q-Q Plot of log-transformed Crystallinity

0.169

Appendix 2. XRF, XRD and thin section analysis results for milled pebbles

Sample No.	%Cu	XRD	Thin Section
2	0.484913	Quartz, muscovite, pyrite or hematite, titanite	
4	0.256437	Quartz, plagioclase (albite), k-feldspar (orthoclase), chlorite (clinochlore), muscovite	
6	0.150986	Quartz, chlorite, muscovite, k-feldspar (sanidine)	
8	0.304369	Quartz, plagioclase (albite), k-feldspar (orthoclase), chlorite (clinochlore), muscovite	
9	0.267621	Quartz, plagioclase (albite), chlorite (chlorite-serpentine), muscovite	
10	1.525839	Quartz, muscovite, chalcopyrite, pyrite	
22	0.166964	Quartz, plagioclase (albite), chlorite (clinochlore), muscovite, k-feldspar (microcline), rutile	
30	0.075094		
31	0.473729		
35	0.561605	Quartz, muscovite, pyrite or hematite, chalcopyrite, tourmaline, titanite	
39	0.107847	Quartz, plagioclase (albite), k-feldspar (orthoclase), chlorite (clinochlore), biotite	
43	1.038529	Quartz, chalcopyrite, muscovite, hematite, orthoferrosilite	
44	0.166165		Quartz, plagioclase, k-feldspar, chlorite, biotite (biotite transformation), chalcopyrite, digenite, covellite, magnetite (large crystals), rutile
45	0.088674	Quartz, chlorite (chlorite-serpentine), k-feldspar (orthoclase), muscovite	
60	0.958642	Quartz, k-feldspar (orthoclase), plagioclase (albite), muscovite, chalcopyrite, tourmaline, rutile, chalcocite	
62	0.950654	Quartz, muscovite, k-feldspar (orthoclase), chalcopyrite	
65	0.363485	Quartz, muscovite, pyrite	
68	0.335525	Quartz, muscovite, hematite, kaolinite	
76	1.589749	Quartz, muscovite, pyrite	
95	0.36029		
97	0.31076	Quartz, muscovite, tourmaline	
101	0.615928	Quartz, muscovite, pyrite or hematite, titanite	

106	0.379463	Quartz, tourmaline, k-feldspar (microcline), plagioclase (albite), muscovite, titanite, chalcocite	
107	1.421986		quartz, muscovite, titanite, molybdenite, fine grained actinolite chalcopyrite
110	0.197321		K-feldspar, plagioclase (feldspar conversion), quartz, chlorite, muscovite chalcopyrite, blue remaining covellite (chalcopyrite conversion), tennanite-tetrahydrite, rutile
119	0.305168		Quartz, sericite, colourless mica, tourmaline, pyrite, chalcopyrite, digenite, covellite, hematite, rutile
125	0.484114		Quartz, sericite, colourless mica, tourmaline, pyrite, chalcocite, digenite, hematite, rutile
128	0.341117	Quartz, muscovite, tourmaline, titanite, chalcopyrite	
137	0.230074	Quartz, pyrite, muscovite, orthoferrosilite	
143	0.089473	Quartz, plagioclase (albite), k-feldspar (orthoclase), chlorite (chlinochlore), muscovite	
145	0.379463	Quartz, pyrite, muscovite	
148	1.070484		

Appendix 3. Confusion matrices of SAM classified images

Sample 76
overall accuracy (27/33) 81.82%
kappa 0.7435

Ground truth (percent)

Class	sulfides	muscovite	tourmaline	musc+tourm	Total
Unclassified	0	0	0	0	0
sulfides	100	11.76	0	0	21.21
muscovite	0	70.59	0	0	36.36
tourmaline	0	17.65	83.33	0	24.24
musc+tourm	0	0	16.67	100	18.12
Total	100	100	100	100	100

Sample 43
overall accuracy (32/36) 88.89%
kappa 0.8581

Ground truth (percent)

Class	musc+tourm	sulfides	muscovite	tourmaline
Unclassified	0	0	0	0
musc+tourm	100	0	20	0
sulfides	0	83.33	0	6.67
muscovite	0	0	80	0
tourmaline	0	16.67	0	93.33
Total	100	100	100	100

Sample 125
overall accuracy 23/33 69.70%
kappa 0.6271

Ground truth (percent)

Class	sulfides	tourmaline	muscovite	musc+tourm	Unclass	Total
sulfide	0	50	0	0	0	3.03
tourmaline	50	50	0	0	0	12.1
muscovite	0	0	94.4	0	0	51.5
musc+tourm	50	0	5.56	100	0	30.3
unclass	0	0	0	0	100	3.03
Total	100	100	100	100	100	100

Sample 60

overall accuracy (27/36) 75.00%

kappa 0.6714

Ground truth (percent)

Class	illite+kaol	muscovite	tourmaline	illite	sulfides	total
illite+kaol	54.55	0	0	18.18	0	22.22
muscovite	9.09	100	0	9.09	0	27.78
tourmaline	0	0	100	0	0	8.33
illite+kaol	36.3	0	0	63.64	0	30.56
sulfides	0	0	0	9.09	100	11.11
total	100	100	100	100	100	100

Sample 22

overall accuracy 26/32 81.25%

kappa 0.7

Ground truth (percent)

Class	chlorite	illite	illite+chl	total
chlorite	85.7	0	0	18.75
illite	0	90.91	28.57	43.75
illite+chl	14.2	9.09	71.4	37.5
total	100	100	100	100

Sample 107

overall accuracy (21/24) 87.50%

kappa 0.6

Ground truth (percent)

Class	muscovite	sulfides	total
muscovite	85.71	0	75
sulfide	14.29	100	25
total	100	100	100

Sample 137

overall accuracy 25/30 83.33

kappa 0.73

Ground truth (percent)

Class	sulfides	muscovite	tourmaline	total
sulfide	50	0	10	13.3
muscovite	33.3	92.86	0	50
tourmaline	16.67	7.14	90	36.67
total	100	100	100	100